Petroleum Science 23 (2026) 3759–3776

Contents lists available at ScienceDirect

Petroleum Science

journal homepage: www.keaipublishing.com/en/journals/petroleum-science

Original Paper

A new insight from morphological numerical simulation of casing shear-compression deformation caused by fault and fracture slip

Hong-Xiang Zhang [a,b], Heng-Mao Tong [b,*], Wen-Hai Ma [c], Nan Zhang [c], Ping Zhang [d], Zi-Ping Liu [e], Peng Wang [c], Shu-Lin Li [f], Yuan Neng [a,b], Cheng-Lin Liu [b], Xue-Song Li [c], Liang Zhang [g]

[a] College of Petroleum, China University of Petroleum-Beijing at Karamay, Karamay, 834000, Xinjiang, China
[b] State Key Laboratory of Petroleum Resources and Engineering, China University of Petroleum (Beijing), Beijing, 102249, China
[c] Production Technology Institute, CNPC Daqing Oilfield Company Limited, Daqing, 163000, Heilongjiang, China
[d] Engineering Technology Department, CNPC Chuanqing Drilling Engineering Company Limited, Chengdu, 610051, Sichuan, China
[e] Oil and Gas Department, CNPC Chuanqing Drilling Engineering Company Limited, Chengdu, 610051, Sichuan, China
[f] Key Laboratory of Shale Gas Exploration, Ministry of Natural Resources (Chongqing Institute of Geology and Mineral Resources), Chongqing, 401120, China
[g] CNPC Tarim Oilfield Company Limited, Korla, 841000, Xinjiang, China

ARTICLE INFO

Article history:
Received 23 January 2024
Received in revised form
27 November 2025
Accepted 16 January 2026
Available online 21 January 2026

Edited by Xi Zhang and Jie Hao

Keywords:
Casing deformation
Unconventional oil and gas
Hydraulic fracturing
Fault and fracture slip
Shear-compression deformation
Displacement attenuation
Finite element numerical simulation

ABSTRACT

The casing shear–compression deformation (CS–CD) caused by well-intersecting small fault and large fracture (F–F) slip induced by hydraulic fracturing is considered to be the main casing deformation (CD) type. The CD morphological characteristics can be clearly recognized using multi-finger imaging tool (MIT) data, but the CS–CD morphological characteristics obtained by existing numerical simulations are far from this, which affects the clarification of CD mechanisms and the formulation of prevention measures. In this paper, the F–F slip kinematic characteristics are analyzed first, and the root of the problem of the traditional displacement uniformity model is revealed: the law that the strata on both F–F sides will undergo movements with displacement attenuation from the F–F plane to both F–F sides during F–F slip is ignored. Then, an improved finite element numerical model is proposed based on this insight, which introduces the displacement attenuation law into the CD analysis for the first time, and the change in the casing drift diameter is proposed as the measurement standard of the CD amount. On this basis, numerical simulations with control variables are carried out to further analyze the relationships between the CD amount and the F–F occurrence parameters, and between the CD amount and the structural and mechanical parameters of the strata, cement sheath and casing. The simulation results demonstrate that: (i) the displacement attenuation model reproduces the morphological characteristics of the actual CS–CD, with displacement attenuation resulting in long CD sections; (ii) the CD amount measurement method based on the casing drift diameter more effectively reflects the actual extent of CD; (iii) increasing the steel grade and wall thickness of the casing is not effective in preventing CD. This paper further elucidates the geomechanical mechanism of CD caused by F–F slip and proposes a CD prevention strategy of controlling F–F activation induced by hydraulic fracturing and using specialized cementing materials to install buffers, thereby providing direct guidance for engineering practice.

1. Introduction

Global unconventional oil and gas (including shale oil and gas, tight oil and gas, etc.) resources are enormous, and their economic and efficient development is crucial to guaranteeing national energy security and stable development. However, the CD

* Corresponding author.
E-mail address: tonghm@cup.edu.cn (H.-M. Tong).
Peer review under the responsibility of China University of Petroleum (Beijing).

https://doi.org/10.1016/j.petsci.2026.01.025
1995-8226/

phenomenon has always been accompanied by the development of unconventional oil and gas using horizontal well hydraulic fracturing technology. CD will prevent the bridge plug from sitting in place during the fracturing operation of subsequent fracturing stages, leading to combined fracturing of multiple stages or even loss of stages. This will not only affect the fracturing reconstruction effect but also increase the operation time and difficulty, ultimately affecting the overall economic benefits of unconventional oil and gas resource development. This has led many scholars to focus their attention on CD research. Although previous studies have argued that the factors causing CD are complex and CD mechanisms are diverse (Daneshy, 2005; Sugden et al., 2012; Shen, 2014; Yu et al., 2014; Jiang et al., 2015; Lian et al., 2015; Tian et al.; Yin and Gao, 2015; Chen et al., 2018; Xi et al., 2018; Yin et al., 2018; Dong et al., 2019; Guo et al., 2019; Xi et al., 2019; Zhang et al., 2020; Li et al., 2021; Zhang et al., 2021b; Shi et al., 2023), the latest studies show that the main CD mechanism is the asymmetric compression of the casing by strata on both F–F sides, caused by the injection of fracturing fluid that leads to the elevation of fluid pressure in well-intersecting F–Fs (the plural form of F–F) and then induces F–F slip during hydraulic fracturing of horizontal wells in unconventional oil and gas reservoirs, and clarify that the resulting CS–CD is the main CD type in the process of hydraulic fracturing in unconventional oil and gas reservoirs at present (Tong et al., 2021b; Zhang et al., 2021a, 2023). In addition, multi-fracture competition and stress interference during hydraulic fracturing will lead to redistribution of the local stress field, resulting in non-uniform slip of fractures (Liu et al., 2023; Zhang et al., 2024), which may also cause CS–CD.

The morphological understanding of CS–CD is crucial for the further clarification of CD mechanisms and the guidance of subsequent CD prevention thoughts. Currently, MIT is the primary method to determine CD morphology. According to the MIT interpretation results, the CS–CD morphology is shown as follows: in the vicinity of the F–F plane, the casing is subjected to asymmetric compression deformation by the shear action of the strata on both F–F sides, resulting in intensive twist and hole shrinkage of the casing and misalignment of the casing axis; far away from the F–F plane, the casing gradually recovers its normal morphology, and the casing axis returns to its original position (Fig. 1).

In addition to using MIT to directly determine CD morphology, finite element numerical simulation software has been widely used by previous researchers to simulate and invert the CS–CD morphology to verify the geomechanical mechanism that F–F slip induces CD (Yin et al., 2018; Guo et al., 2019; Xi et al., 2019; Zhang et al., 2020; Shi et al., 2023). However, through investigation, we found that predecessors had the following problems in relevant numerical simulations: (i) they consider that when F–F slip causes CD, only the strata on one F–F side move, the strata on another F–F side are fixed, and the stratum displacements of the F–F moving side are equal everywhere (Yin et al., 2018; Xi et al., 2019; Zhang et al., 2020). Although the local CS–CD characteristics are simulated according to this thought, the overall CD morphology, where the casing axis shows overall misalignment characteristics, is far from the actual morphology. (ii) According to the above simulation, they consider that CD occurs only at the intersection with the F–F plane, and the CD amount is the change in the local casing inner diameter (i.e., the casing minimum inscribed circle diameter) at the intersection between the casing and the F–F plane before and after CD (Zhang et al., 2020). The problem with this understanding is that on the one hand, the simulated CD section is only a few tens of centimeters long, which cannot explain the actual several meters or even a dozen meters long CD section (Fig. 2), and on the other hand, the downhole pipe string tool (mainly including the bridge plug and perforation gun) during hydraulic fracturing is up to several meters long, and the external diameter is not equal, so the CD amount should be the change in the casing drift diameter that allows the pipe string tool to pass through (i.e., the diameter of the casing inscribed cylinder, which the entire pipe string tool is regarded as) (Fig. 3). Therefore, the CD amount measured by the change in local casing inscribed circle diameter (AA′–CC′) will be obviously smaller than the actual CD amount (AA′–BB′), as shown in Fig. 3. This misunderstanding also exists in the CD amount measurement through MIT in the field. (iii) They consider that when multiple F–Fs slip simultaneously, the strata sandwiched by the F–Fs undergo stepped dislocation, and the stratum displacements of the F–F moving side are similarly equal everywhere (Guo et al., 2019; Shi et al., 2023). The problem with this understanding is that the CD morphology simulated under this simulation thought is inconsistent with the actual morphology, and the F–F slip characteristics violate the mechanical mechanism, i.e., two parallel F–Fs, at a distance of only a few meters from each other, occur diametrically opposite slip.

The physical simulation experimental method corresponding to the numerical simulation is also widely used in the study of CD mechanism (Cao et al., 2022; Yang et al., 2023). However, due to the limitations of technical conditions and simulation scale, the physical simulation experiment also cannot realize the displacement attenuation of the strata on both F–F sides. Besides, the physical simulation experiment can only set the F–F and casing to a perpendicular state, which cannot realize the change of the F–F occurrence. Compared with numerical simulation, the physical simulation experiment has greater limitations in this study.

In view of the above problems related to the boundary condition settings of the CS–CD numerical simulation and the casing morphology characteristics in the simulation results, this paper

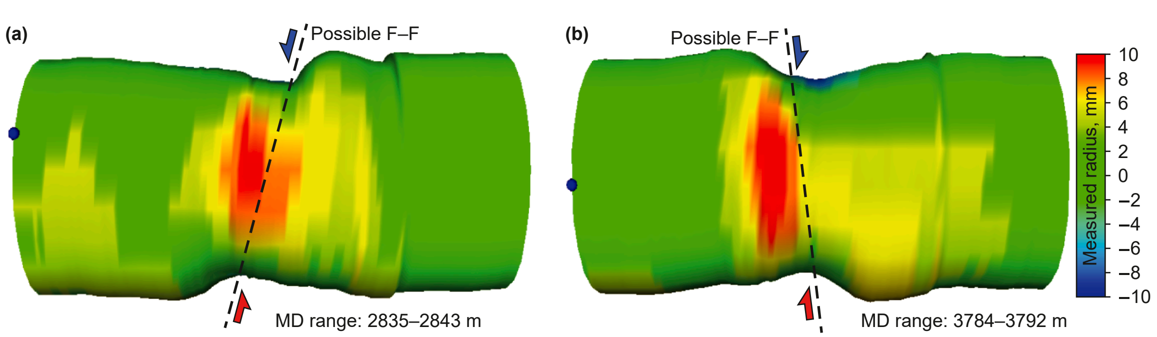

Fig. 1. CS–CD shown by MIT-24 interpretation results (modified after Tong et al., 2021b; Zhang et al., 2023). (**a**) 3D morphology of MIT-24 interpretation in the 2835–2843 m section of well W2H13-1. (**b**) 3D morphology of MIT-24 interpretation in the 3784–3792 m section of well W4H12-2. The measured radius color scale in the figure refers to the difference between the measured radius of the 24 fingers and the casing original radius. The casing original radius is 57.15 mm, the measured radius equal to this value corresponds to 0 in the color scale, the measured radius greater than this value corresponds to a positive value in the color scale, and the measured radius less than this value corresponds to a negative value in the color scale.

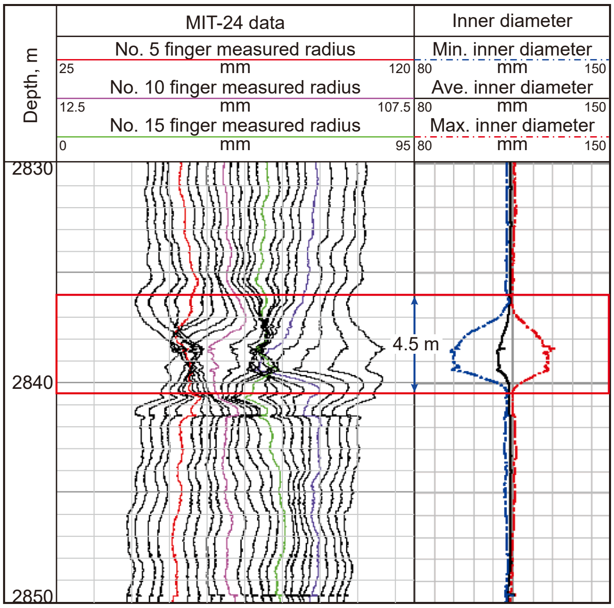

Fig. 2. Curve graph of MIT-24 in the 2830–2850 m section of well W2H13-1. This CD section ranges from 2836 to 2840.5 m and is 4.5 m long.

first deeply analyzes and discusses the F–F slip kinematic characteristics and reveals the displacement attenuation law of the strata on both F–F sides. On this basis, displacement attenuation law is introduced into the CS–CD numerical simulation for the first time, which solves the problems of mismatch of CD morphology and too short CD length in traditional models. A CD measurement method based on the casing drift diameter is proposed, which corrects the misunderstanding that focuses exclusively on localized hole shrinkage of the casing. Furthermore, the relationship between the CD amount and the relevant influence factors is analyzed, which points out the reason why the increase of the steel grade and wall thickness of the casing is ineffective in preventing CD. The research results further clarify the CD mechanism and can provide important reference and guidance for the CD prevention.

2. Analysis of the F–F slip kinematic characteristics

Analyzing the CS–CD simulations conducted by predecessors, we find that the root cause of problems in the simulation results is the misunderstanding of the F–F slip kinematic characteristics.

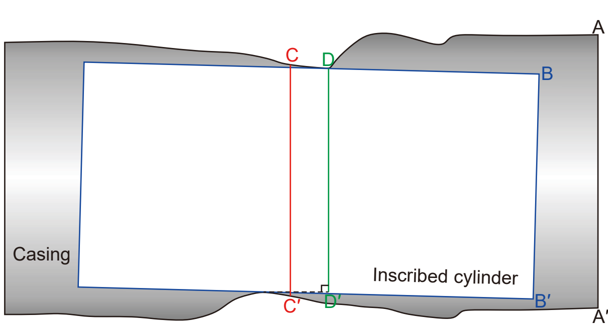

Fig. 3. Schematic diagram of the casing profile tracing, casing minimum inscribed circle diameter and inscribed cylinder diameter in the 2835–2843 m section of well W2H13-1. In this figure, AA′ is the casing original inner diameter, BB′ is the casing inscribed cylinder diameter, CC′ is the casing minimum inscribed circle diameter, and DD′ is the vertical distance between the two points with the closest vertical distance on the casing inner wall.

Therefore, we first analyze and discuss the kinematic characteristics of the strata on both F–F sides during F–F slip to provide reasonable boundary load conditions for the subsequent simulations.

When the shear stress on the F–F plane overcomes the cohesion and friction on the F–F plane, the strata on both F–F sides will shear slip along the F–F plane (Tong et al., 2010, 2015; Tong and Yin, 2011). Theoretical models of the movements of the strata on both F–F sides during F–F slip given in existing structural geology textbooks (Van Der Pluijm and Marshak, 2004; Twiss and Moores, 2007; Davis et al., 2011; Fossen, 2016) are mostly the overall dislocation of the strata on both F–F sides (the displacements of the strata on both F–F sides are equal in magnitude and opposite in direction everywhere). However, since the effect of actual faulting on the displacements of the strata on both F–F sides cannot be infinitely distant due to spatial constraints, this theoretical model is obviously not in line with the actual geological situation. Through systematic literature research, we find that there is still a lack of clear and definite understanding of the specific displacement distribution of the strata on both F–F sides during F–F slip. Therefore, this paper explores and analyzes the displacement distribution characteristics of the strata on both F–F sides during F–F slip by simple numerical simulations and finds two important laws: (i) the strata on both F–F sides move simultaneously, i.e., the strata on both F–F sides are active; (ii) the stratum displacement attenuation on both F–F sides exists in the direction perpendicular to the F–F plane.

2.1. Simultaneous movements of the strata on both F–F sides

We first designed six simple 2D plane strain conceptual models (Fig. 4) to explore these problems. All six models are 500 m × 500 m squares with a material having a Young's modulus of 20 GPa and a Poisson's ratio of 0.25. Models 1, 3, and 5 are set with an F–F at an angle of 60° to the X direction and a length of 100 m in the center of squares, and a frictional contact is set between the strata on both F–F sides with a friction coefficient of 0.6, while models 2, 4, and 6 serve as comparison models with no F–F. All six models are set with normal constraints at the square boundaries in the X direction. Models 1 and 2 are set with normal constraints at the lower boundary of squares and displacement loads of −200 mm (the negative sign means that the displacement points to the negative half axis of the Y direction) at the upper boundary to simulate the tectonic action situation of unilateral compression. Models 3 and 4 are set with displacement loads both at the upper and lower boundaries of squares, with displacements of −100 mm and 100 mm respectively, to simulate the tectonic action situation of bilateral compression. Models 5 and 6 are set with normal constraints both at the upper and lower boundaries of squares and geostress loads of 50 MPa in the X direction and 60 MPa in the Y direction to simulate the tectonic action situation of known stress states. The above model parameters are set with reference to the actual geological conditions of a certain area. Since gravity is not considered, it can be considered that all six models are in strike-slip stress states. In addition, models 1 and 2, 3 and 4, and 5 and 6 are compared with each other to eliminate the effect of stratum displacements caused by non-F–F slip.

As shown in Fig. 5, the simulation result of model 1 shows that the displacement at the F–F plane center on the F–F left side is −90.1 mm, and the displacement at the F–F plane center on the F–F right side is −110.2 mm. In the simulation result of model 2, the displacement at the center of the hypothetical F–F plane (the dashed line in Fig. 5(b)) is −100.0 mm, which is the stratum

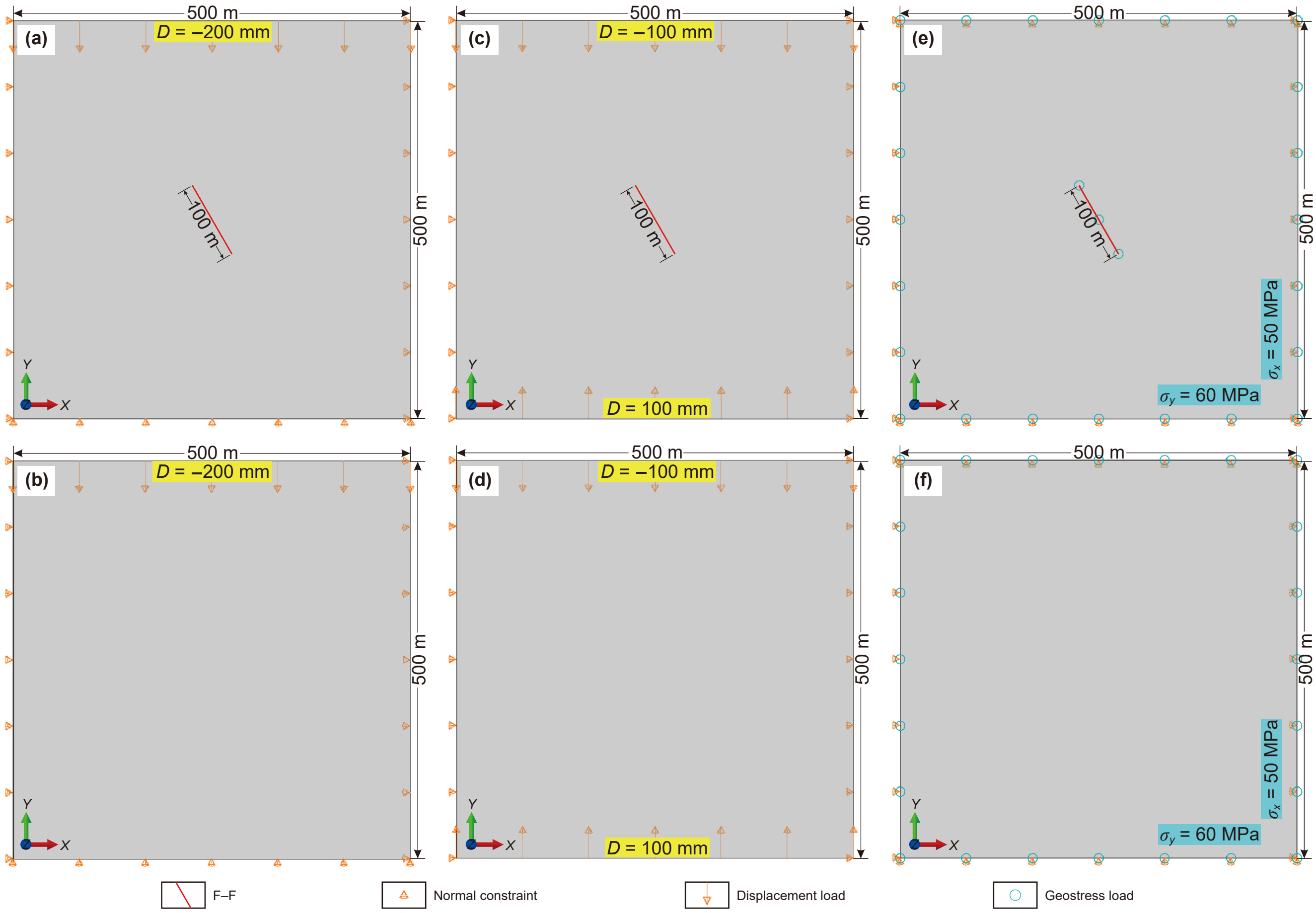

Fig. 4. Structure and boundary load settings of 2D plane strain conceptual models of F–F slip under strike-slip stress states. (**a**) Model 1. (**b**) Model 2. (**c**) Model 3. (**d**) Model 4. (**e**) Model 5. (**f**) Model 6. In the figure, D is the loading displacement, and σ_x and σ_y are the geostresses in the X and Y directions respectively.

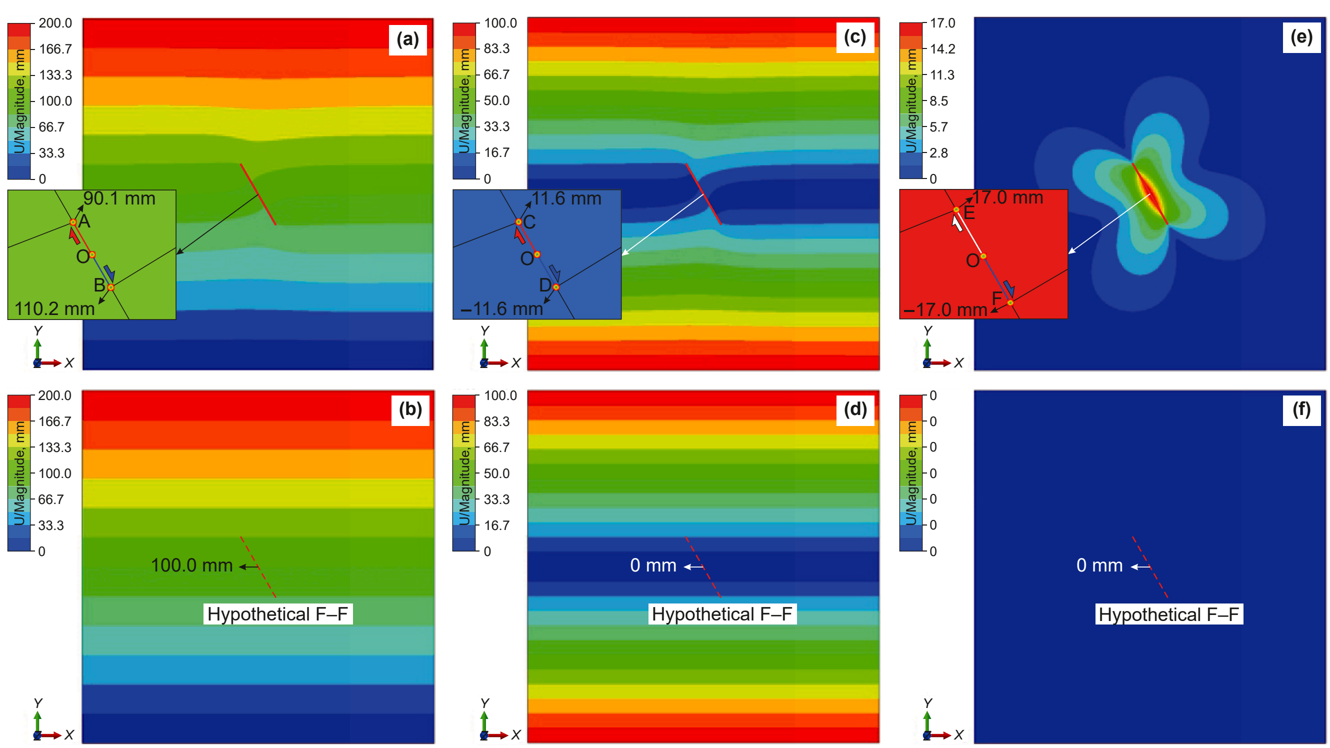

Fig. 5. Displacement magnitude distribution graphs in the simulation results of 2D plane strain conceptual models of F–F slip under strike-slip stress states. (**a**) Model 1. (**b**) Model 2. (**c**) Model 3. (**d**) Model 4. (**e**) Model 5. (**f**) Model 6. In the figure, “U/Magnitude” is the displacement magnitude.

displacement at the F–F plane centers on both F–F sides caused by non-F–F slip in model 1. It should be noted here that the displacements at the F–F plane centers on both F–F sides in model 1 are parallel to the F–F plane, whereas the displacement of the center of the hypothetical F–F plane in model 2 is parallel to the *Y* direction. Therefore, a trigonometric transformation is needed to eliminate the stratum displacement caused by non-F–F slip in model 1. After eliminating the stratum displacement caused by non-F–F slip in model 1, the displacement at the F–F plane center on the F–F left side is 11.6 mm (OA in Fig. 5(a)), and the displacement at the F–F plane center on the F–F right side is −11.6 mm (OB in Fig. 5(a)). Similarly, after eliminating the stratum displacement caused by non-F–F slip, the displacements at the F–F plane center on the F–F left side in models 3 and 5 are 11.6 mm (OC in Fig. 5(c)) and 17.0 mm (OE in Fig. 5(e)) respectively, and the displacements at the F–F plane center on the F–F right side in models 3 and 5 are −11.6 mm (OD in Fig. 5(c)) and −17.0 mm (OF in Fig. 5(e)) respectively.

The above simulation results show that regardless of which loading method is adopted, the strata on both F–F sides will move simultaneously along the F–F plane as long as the F–F slip condition is reached. When the F–F slip manifests itself as strike-slip fault activity in the above model, the slip displacements at the F–F plane corresponding points of the strata on both F–F sides are equal in magnitude and opposite in direction. However, when the F–F slip manifests itself as normal or reverse fault activity, the displacement magnitude at the F–F plane corresponding points of the F–F ascending and descending walls will differ due to the incorporation of gravity. Similarly, we designed four more simple 2D plane strain conceptual models to illustrate this problem.

As shown in Fig. 6, the same structural and material mechanical parameter settings as in Fig. 5 are used for the four models. Among them, models 7 and 9 are set with an F–F and frictional contact between the strata on both F–F sides, while models 8 and 10 serve as comparison models with no F–F. Since gravity needs to be taken into consideration when normal or reverse faults slip, the material

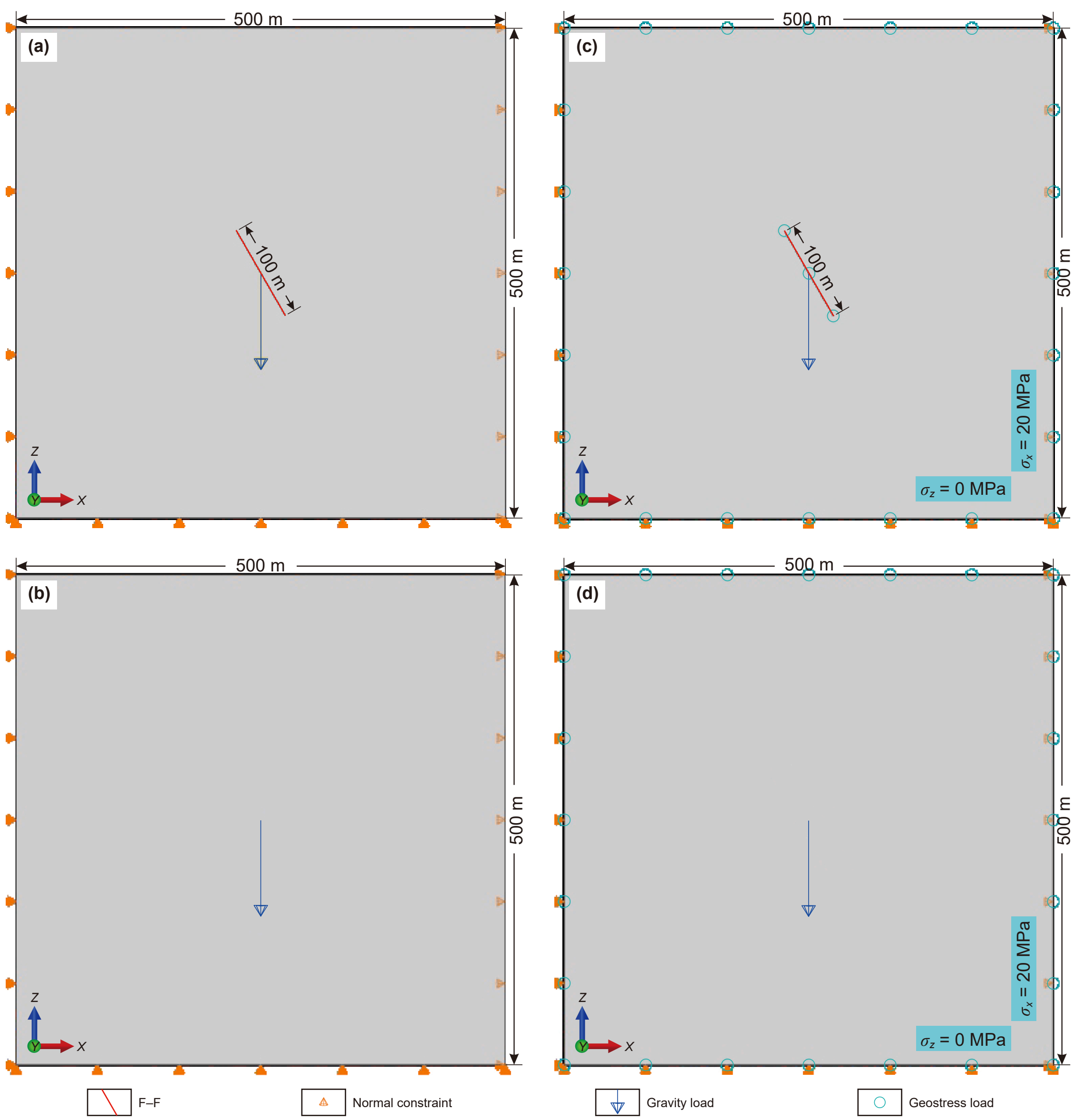

Fig. 6. Structure and boundary load settings of 2D plane strain conceptual models of F–F slip under extension and compression stress states. (**a**) Model 7. (**b**) Model 8. (**c**) Model 9. (**d**) Model 10. In the figure, σ_x and σ_z are the geostresses in the *X* and *Z* directions respectively.

density of squares is set to 3 g/cm^3. In addition, for all four models, normal constraints are set at the square boundaries in the *X* direction and the square lower boundary, while the square upper boundary is a free boundary. Models 7 and 8 are only set with gravity loads to simulate the situation of normal fault slip, while models 9 and 10 are set with both gravity loads and geostress loads of 20 MPa in the *X* direction to simulate the situation of reverse fault slip. Models 7 and 8, and 9 and 10 are compared with each other to eliminate the effect of stratum displacements caused by non-F–F slip.

As shown in Fig. 7, after eliminating the stratum displacement caused by non-F–F slip, the displacements at the F–F plane center on the F–F hanging wall in models 7 and 9 are 8.6 mm (OG in Fig. 7(a)) and 31.0 mm (OI in Fig. 7(c)) respectively, and the displacements at the F–F plane center on the F–F footwall in models 7 and 9 are −7.6 mm (OH in Fig. 7(a), the negative sign means that the displacement points to the negative half axis of the *Z* direction) and −27.8 mm (OJ in Fig. 7(c)) respectively, so the differences in the displacement magnitude at the F–F plane centers on both F–F sides in models 7 and 9 are 1.0 mm and 3.2 mm respectively. It should be noted here that since the difference in the displacement magnitude at the corresponding points on both F–F sides in Model 9 is mainly caused by the geostress loads in the *X* direction and the free boundary at the square upper boundary and the gravity loads only decrease the difference in the displacement magnitude, the change in the difference in the displacement magnitude at the corresponding points on both F–F sides before and after the gravity loads should be compared in studying the gravity effect on the displacements of both F–F sides. As shown in Fig. 7(e), before the gravity loads in model 9, the displacement at the F–F plane center on the F–F hanging wall is 39.7 mm (OK in Fig. 7(e)), the displacement at the F–F plane center on the F–F footwall is −35.4 mm (OL in Fig. 7(e)), and the difference in the displacement magnitude at the F–F plane centers on both F–F sides is 4.3 mm (the stratum displacement caused by non-F–F slip is 0). Then, the change in the difference in the displacement magnitude at the F–F plane centers of the strata on both F–F sides before and after the gravity loads is 1.1 mm.

This indicates that the gravity effect on the displacement of the descending wall is greater than that of the ascending wall, whether during normal or reverse fault slip, which makes the displacement at the corresponding point on the descending wall larger than that on the ascending wall for normal faults, and the difference in the displacement magnitude at the corresponding points of the strata on both F–F sides is smaller compared to that in the absence of gravity load for reverse faults. The main reason for this phenomenon is that the vertical stress gradient generated by gravity makes the flexural resistance overcome by the ascending wall (equivalent to lifting the strata upward) larger than that of the descending wall (equivalent to pulling the strata downward). However, for F–Fs causing CS–CD, even if the F–F slip manifests itself as normal or reverse fault activity, the displacement magnitude of the strata on both F–F sides is mostly a few centimeters and the difference is only a few millimeters, which has little effect on the CD morphology simulations and can be ignored. Therefore, we only need to pay attention to the law that the strata on both F–F sides will move simultaneously along the F–F plane during F–F slip.

2.2. Displacement attenuation in the direction perpendicular to the F–F plane

When F–F slips, the strata on both F–F sides are not infinitely offset. The actual F–F plane is a surface with a finite area, where the displacement is the largest at the F–F plane center and gradually attenuates to 0 to the F–F plane periphery (Fig. 8). Fossen briefly discussed the phenomenon that the stratum displacement from the center to the tip of the fault plane gradually attenuates to

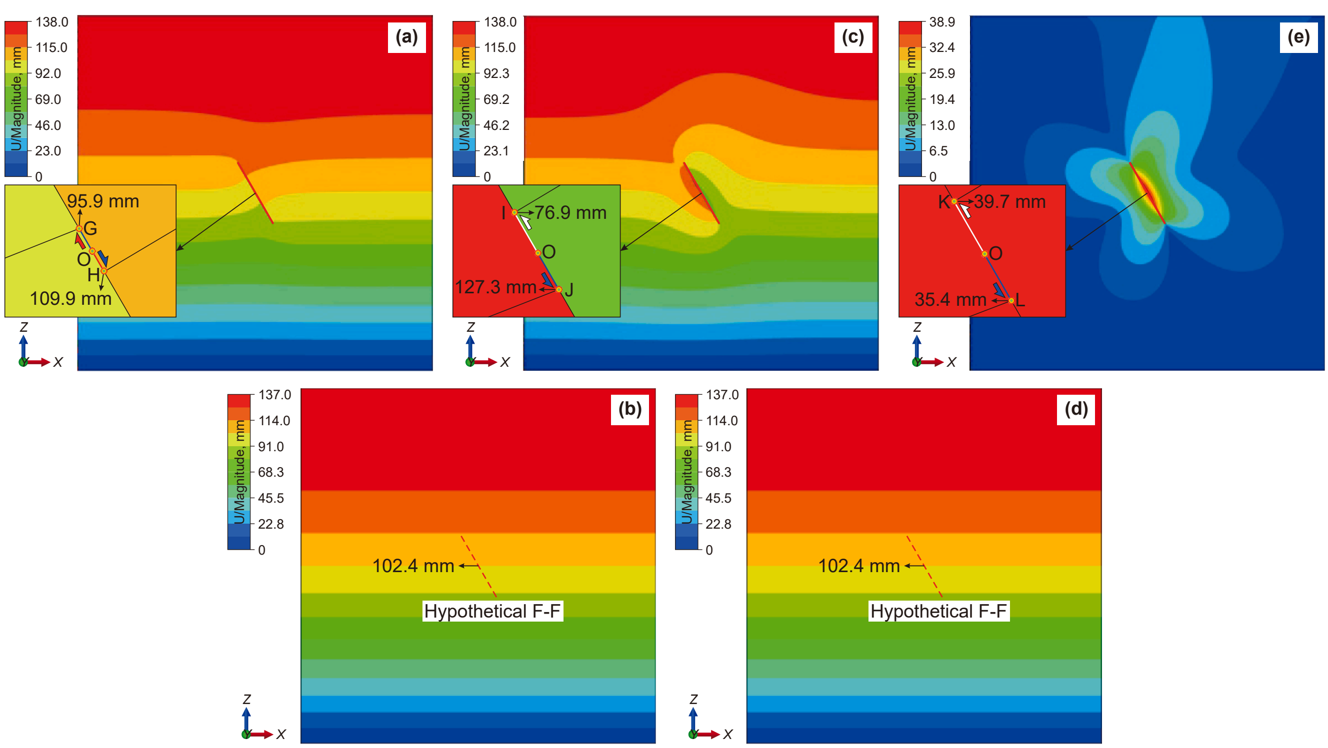

Fig. 7. Displacement magnitude distribution graphs in the simulation results of 2D plane strain conceptual models of F–F slip under extension and compression stress states. (**a**) Model 7. (**b**) Model 8. (**c**) Model 9. (**d**) Model 10. (**e**) Model 9 without gravity load.

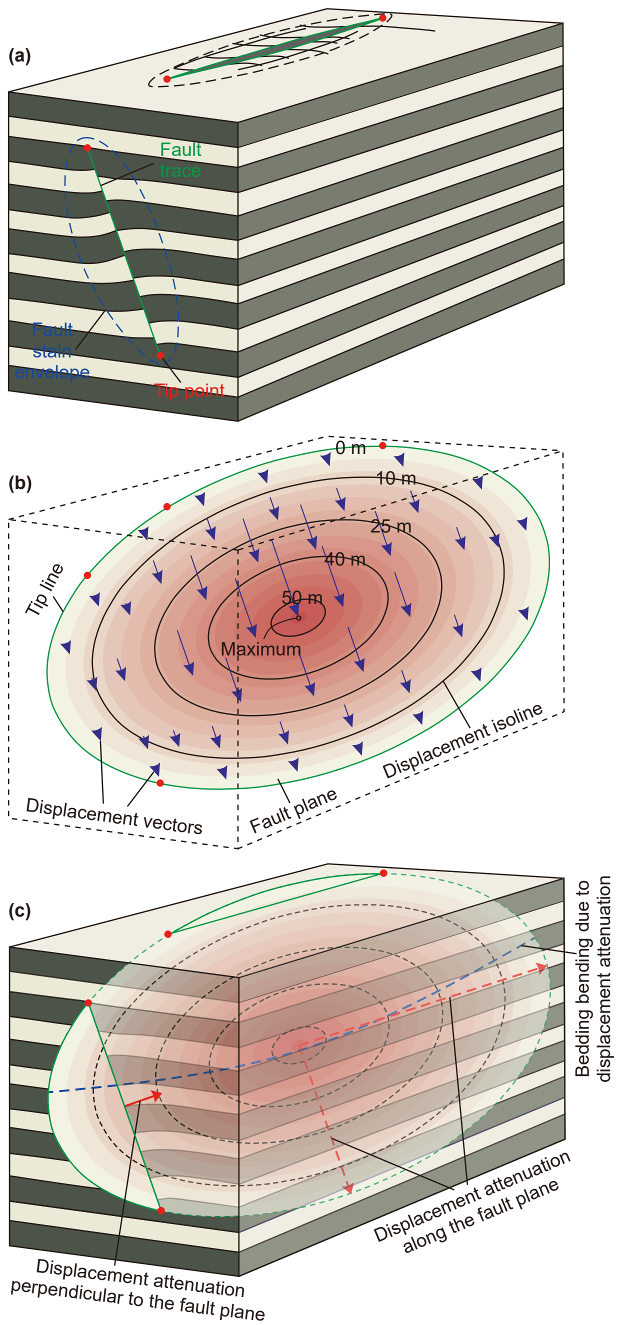

Fig. 8. Geometric characteristics of an isolated elliptical fault (modified after Fossen, 2016). (**a**) The stratum displacement gradually attenuates to 0 from the center to the tip points of the fault plane, leading to the strata around the fault bending to form a displacement-induced drag structure. The fault trace is the intersection between the fault plane and an arbitrary surface, the tip point is the endpoint of the fault trace, and the fault strain envelope indicates the range of the stratum strain on both fault sides. (**b**) This displacement attenuation from the center to the tip line of the fault plane can be expressed in terms of displacement contours and displacement vectors. The tip line is the collection of tip points, which is the zero-displacement line that outlines the fault. (**c**) The manifestation of stratum displacement attenuation in the direction along the fault plane and perpendicular to the fault plane.

0 along the direction of the fault plane, resulting in the strata around the fault bending to form a displacement-induced drag structure (Fig. 8(a)) in the book Structural Geology, 2nd edition (Fossen, 2016). Although Fossen did not explicitly state the stratum displacement attenuation from the fault plane to both fault sides in the direction perpendicular to the fault plane, and no other relevant literature has discussed this phenomenon, the phenomenon that the stratum bending extent gradually decreases and disappears as away from the fault plane in Fig. 8(a) has implied this characteristic, i.e., this displacement attenuation not only manifests in the direction along the fault plane but also in the direction perpendicular to the fault plane.

Due to the presence of the fault plane, stress concentration will occur near the plane in a geological body under geostress. When the shear stress exceeds the cohesion and friction on the fault plane, the strata around the fault plane will shear slip along the fault plane (Fig. 5(e)) (Tong et al., 2010, 2015; Tong and Yin, 2011). In contrast, for areas distant from the fault plane that are not affected by the fault and maintain an unchanged stress state, the strata remain undeformed and cannot move along with these around the fault plane due to spatial constraints of the surrounding strata. This leads to the phenomenon that the stratum displacement gradually attenuates to 0 from the center to the tip of the fault in the direction along the fault plane, and from the fault to both sides in the direction perpendicular to the fault plane. Spatially, this manifests as flexure of the strata around the fault plane, forming a so-called displacement-induced drag structure (Fig. 8(a)). As the strata bend, the geological body eventually reaches a new state of stress equilibrium, and the movement of the strata on both fault sides ceases accordingly. Besides, the phenomenon that the strata on both fault sides show displacement attenuation in the direction perpendicular to the fault plane further illustrates that the strata on both fault sides will move simultaneously along the fault plane during fault slip.

In fact, this physical phenomenon is widespread in nature and can be observed in both field outcrops and seismic data. It applies not only to small F–Fs (Fig. 9(a)) but also to large faults in basins (Fig. 9(b)). However, limited by observation scale, observation angle and seismic data resolution, this phenomenon often cannot manifest itself clearly and is thus neglected. In addition, for large faults at basin boundaries and small F–Fs exposed on the surface, the displacement change laws along the fault or F–F plane may be more complicated due to the influence of fault connection, lack of surrounding stratum limitation, change in fault occurrence and isostasy, but in the direction perpendicular to the fault or F–F plane, the displacement attenuation from the fault or F–F plane to both fault or F–F sides always exists. Of course, different faults or F–Fs have different displacement attenuation laws in the direction perpendicular to the fault or F–F plane, but this is not the focus of this paper and will be discussed in another paper.

The above analysis shows that the strata on both F–F sides will undergo movements with displacement attenuation from the F–F plane to both F–F sides during F–F slip. The F–F slip kinematic characteristics are widespread and should naturally be true for the F–F slip that causes CS–CD. Therefore, the characteristics should be taken into consideration when CS–CD numerical simulations are carried out. Besides, this insight can provide ideas for in-depth research on basic structural issues such as the formation mechanism of basin peripheral uplifts, foreland basins and traction and reverse traction structures.

It should be noted that the above F–F slip kinematic characteristics are a simple geological understanding, which is easier to understand and except for geological professionals, but it is also easy to be ignored. Moreover, the above CS–CD numerical simulations are mostly carried out by engineering professionals. This is the most important reason why no relevant research has ever taken the characteristics as model boundary conditions.

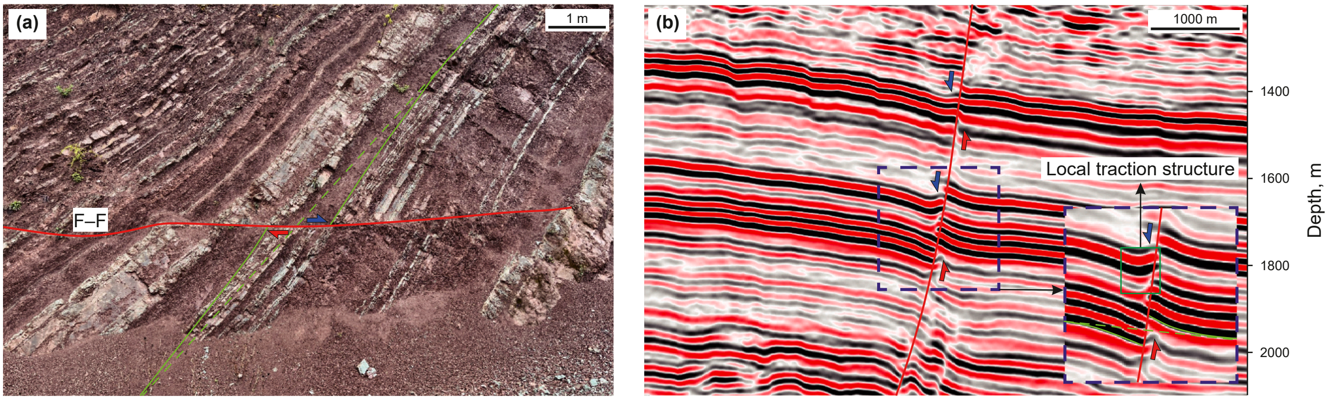

Fig. 9. The phenomenon of stratum displacement attenuation from the fault or F–F plane to both fault or F–F sides in small F–Fs in field outcrops and large faults in seismic profiles. (**a**) A small F–F pinches out on the right side of the figure in a field outcrop in a certain area of the Sichuan Basin. In the direction perpendicular to the F–F plane, the stratum displacement attenuation characteristics are obvious. (**b**) A normal fault dislocates all seismic events in a seismic profile in the Gulong block of the Songliao Basin. Small traction structures form locally near the fault planes due to the stratum drag effect, but the overall stratum displacement attenuation is still shown in the direction perpendicular to the fault plane.

3. Numerical simulation of CS–CD morphology

According to the above F–F slip kinematic characteristics, we established a 3D finite element coupling model consisting of strata, F–F, cement sheath and casing to simulate CS–CD morphology. On this basis, we conducted control variable simulations with different F–F occurrence parameters and the structural and mechanical parameters of strata, cement sheath and casing to analyze the relationships between CD amount and these parameters, which can provide a further basis for CD mechanism clarification and CD prevention.

The simulations are carried out with the example of F–F slip of normal fault properties, and the morphology characteristics of CS–CD due to F–F slip of strike-slip and reverse fault properties are consistent with them. The resulting laws and understandings are also universal.

3.1. Software platform and constitutive equation

In this paper, Abaqus/Standard 2021 is used to conduct 3D finite element numerical simulation, and the model is constructed based on the generalized Hooke's law, Von Mises criterion and Coulomb friction model as the constitutive equation.

The strata and cement sheath are simplified as isotropic linear elastomers, and the generalized Hooke's law (Timoshenko and Goodier, 1951; Jaeger et al., 2007) is adopted to describe their stress-strain relationship. The expression of the generalized Hooke's law is:

$$\sigma_{ij} = \frac{E}{1+\nu}\varepsilon_{ij} + \delta_{ij}\frac{\upsilon E}{(1+\upsilon)(1-2\upsilon)}\sum_k \varepsilon_{kk}, i,j = 1,2,3 \tag{1}$$

$$\delta_{ij} = \begin{cases} 1, i = j \\ 0, i \neq j \end{cases}$$

where σ_{ij} is the stress tensor component; ε_{ij} is the strain tensor component; E is the Young's modulus; υ is the Poisson's ratio.

The Von Mises criterion (Hill, 1950) is adopted to describe the elastoplastic behavior of the casing with the following expression:

$$2\sigma_s^2 = (\sigma_1 - \sigma_2)^2 + (\sigma_2 - \sigma_3)^2 + (\sigma_1 - \sigma_3)^2 \tag{2}$$

where σ_s is the yield strength; σ_1, σ_2, σ_3 are the maximum, intermediate, and minimum principal stresses respectively.

The Coulomb friction model (Jaeger et al., 2007) is used to describe the friction contact behavior in the model, and its expression is:

$$\tau = \mu\sigma_n \tag{3}$$

where τ is the friction stress; σ_n is the normal stress; μ is the friction coefficient.

3.2. Model structure

The model consists of four parts: strata, F–F, cement sheath and casing (Fig. 10). The strata are divided equally into the hanging wall and the footwall in the extension direction, with overall dimensions of 6 m × 1 m × 1 m. The interior of the strata is hollow and filled with cement sheath and casing. The F–F is located between the hanging wall and the footwall. The F–F slip amount (D), the angle (α) between the F–F strike and the well trajectory (depending on the F–F inclination), and the F–F dip angle (φ) are model variables. When α and φ are not taken as variables, their values are 90° and 60° respectively. The cement sheath is located between the strata and the casing, of which the wall thickness (L_1) is a model variable. When L_1 is not taken as a variable, its value is 38.1 mm. The casing is located at the innermost part of the model and has an inner diameter of 118.62 mm, of which the wall thickness (L_2) is a model variable. When L_2 is not taken as a variable, its value is 10.54 mm. The value range of each model structural parameter variable is shown in Table 1. The parameter values are based on actual geological and engineering data: the values of the F–F slip amount refer to the measured CD amount data, the values of the angle between the F–F strike and the well trajectory and the F–F dip angle refer to the statistical results of the F–F occurrence in the Weiyuan block, and the values of the cement sheath and casing structure parameters refers to the commonly used wellbore-cement sheath-casing dimensions in the field.

In addition, to simulate the CS–CD morphology in the case of multiple F–Fs simultaneously slipping, we also designed two models with two identically inclined F–Fs and two oppositely inclined F–Fs (Fig. 11). Except for changes in the overall length of the two models to better represent the CD morphology, all remaining

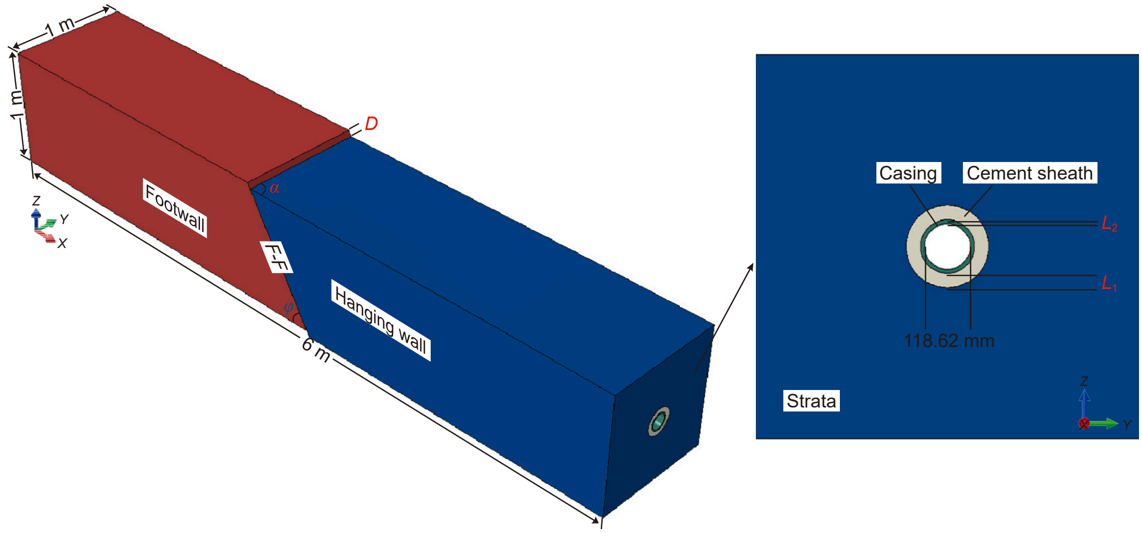

Fig. 10. Structure of the finite element coupling model consisting of strata, F–F, cement sheath and casing.

Table 1
Structural parameter settings of CS–CD models.

D, mm	A, °	φ, °	L_1, mm	L_2, mm
10	15	15	38.1	10.54
20	30	30	40	12
30	45	45	45	14
40	60	60	50	16
50	75	75	55	18
	90	90	60	20

parameters (including material mechanical parameters) are taken as non-model variables.

3.3. Material mechanical parameter

The Young's modulus (E_1) and Poisson's ratio (υ_1) of the strata are model variables. When E_1 and υ_1 are not taken as variables, their values are 20 GPa and 0.3 respectively. The Young's modulus (E_2) and Poisson's ratio (υ_2) of the cement sheath are model variables. When E_2 and υ_2 are not taken as variables, their values are 10 GPa and 0.25 respectively. The yield strength (σ_s) of the casing is a model variable. When σ_s is not taken as a variable, its value is 864 MPa. In addition, the values of the Young's modulus and Poisson's ratio of the casing are 210 GPa and 0.3 respectively. The value range of each model material parameter variable is shown in Table 2. The parameter values are based on actual geological and engineering data: the values of the Young's modulus and Poisson's ratio of the strata refer to the conventional shale elastic parameter test data, the values of the Young's modulus and Poisson's ratio of the cement sheath refer to the mechanical properties of cement commonly used in the field (API standard), and the values of the yield strength, Young's modulus and Poisson's ratio of the casing refer to the mechanical properties of the casing with P110 steel grade commonly used in the field.

3.4. Contact relationship

The contact relationships in the model include the contact relationships between the hanging wall and footwall, between the hanging wall and footwall and the cement sheath, and between the cement sheath and the casing. The contact relationships are all set as frictional contact with a friction coefficient of 0.6 with reference to actual geological conditions.

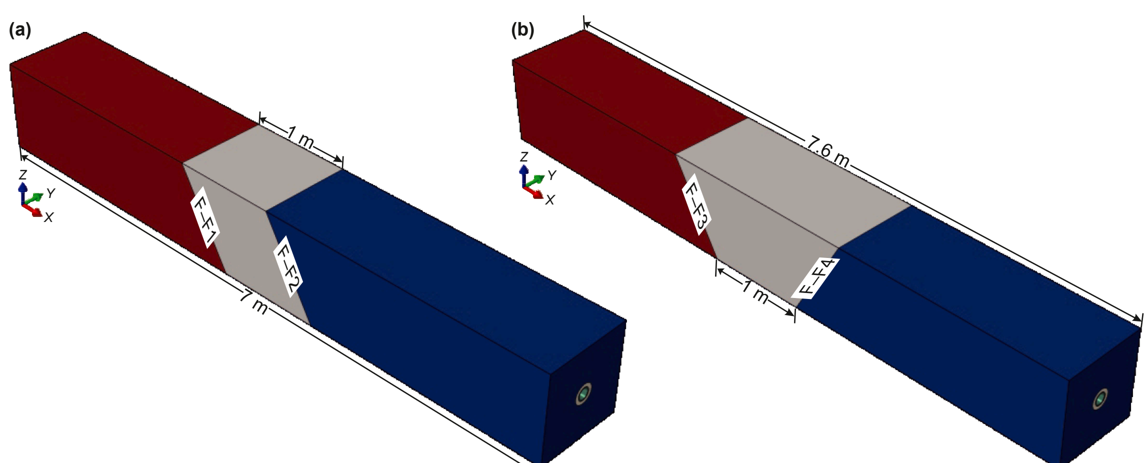

Fig. 11. Structure of double F–F models. (**a**) Model with two identically inclined F–Fs. (**b**) Model with two oppositely inclined F–Fs.

Table 2
Material parameter settings of CS–CD models.

E_1, GPa	υ_1	E_2, GPa	υ_2	σ_s, MPa
20	0.2	0.1	0.22	800
25	0.22	1	0.24	850
30	0.24	2	0.25	864
35	0.26	4	0.26	900
40	0.28	6	0.28	950
	0.3	8	0.3	1000
		10		

3.5. Loading method

The main consideration for the loading method settings is how the stratum displacements on both F–F sides are loaded.

Since displacement attenuation was not considered in the simulations performed by predecessors, we first designed a model with a uniform displacement load to facilitate the comparison. In this model, the strata on both F–F sides slip along the direction parallel to the F–F tilt, and the displacements at each point of the strata are the same in both magnitude and direction on the same F–F side and are equal in magnitude and opposite in direction on different F–F sides (Fig. 12(a)). We call the loading method in this model the displacement uniformity mode. It should be noted that all displacement loads are applied to the upper and lower boundaries of the strata, and displacement loads are not set at the inner and lateral boundaries of the strata, the same as below. The reason for this setting is that the displacement change of the strata on both F–F sides along the F–F plane is naturally caused by the presence of the cement sheath and casing. Moreover, the remaining outer boundaries of the strata are set with normal constraints to keep the overall model stable during F–F slip, the same as below. The remaining parameters of this model are taken as non-model variables.

Then, based on the above understanding of the F–F slip kinematic characteristics, we designed the following model loading method: The strata on both F–F sides also slip along the direction parallel to the F–F tilt, but the displacements of the strata on both F–F sides are equal in magnitude and opposite in direction at the corresponding points symmetric about the F–F plane center. Due to the small F–F scale in the model, the displacements at each point of the strata on the same F–F side are uniformly distributed in the direction of the F–F strike and gradually attenuate in the direction perpendicular to the F–F plane, i.e., the farther away from the F–F plane, the smaller the stratum displacements are, until they attenuate to 0. We call this loading method the displacement attenuation mode. As mentioned before, displacement attenuation has different attenuation laws, such as linear attenuation and quadratic attenuation, and the position of the attenuation to 0 is also different. We define the horizontal distance between the F–F plane and the position where the stratum displacements attenuate to 0 as the displacement attenuation distance, which determines the displacement attenuation rate. With different displacement attenuation laws, the simulated CD amount and CD length (total length of the deformed casing) will also be different. Here, we simplify the displacement attenuation mode to linear attenuation with a displacement attenuation distance of 1 m (Fig. 12(b)). To illustrate the influence of the displacement attenuation rate on the CD length, we also designed a model with a displacement attenuation distance of 2 m. The remaining parameters of the two model are taken as non-model variables.

In addition, the above simulations with control variables all adopt the displacement attenuation mode with a displacement attenuation distance of 2 m for the boundary load. For the above two double F–F models, the displacement attenuation mode with a displacement attenuation distance shown in Fig. 13 is also adopted for the boundary load.

3.6. Mesh division

The mesh node spacings of the strata are set to 100 mm, and the strata are divided into four parts from the outer boundaries to the inner cylinder to achieve a gradual tightening of meshes from the outside to the inside (Fig. 14(a)). The axial mesh node spacings of

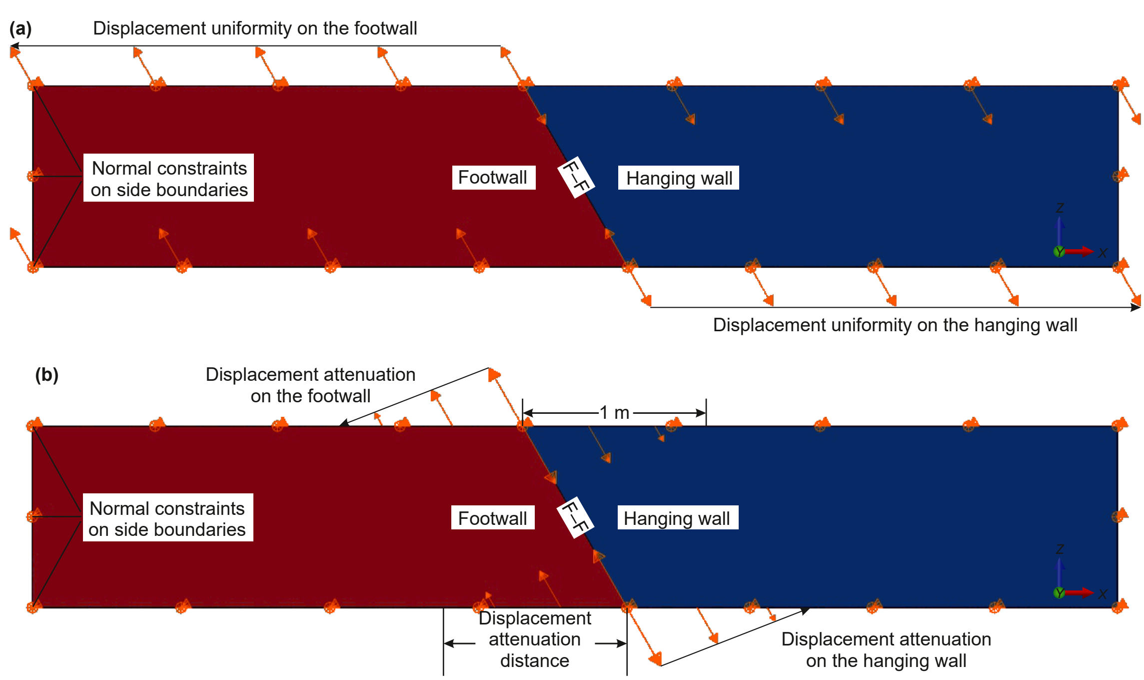

Fig. 12. Comparison of different model loading methods. (**a**) Displacement uniformity mode. (**b**) Displacement attenuation mode.

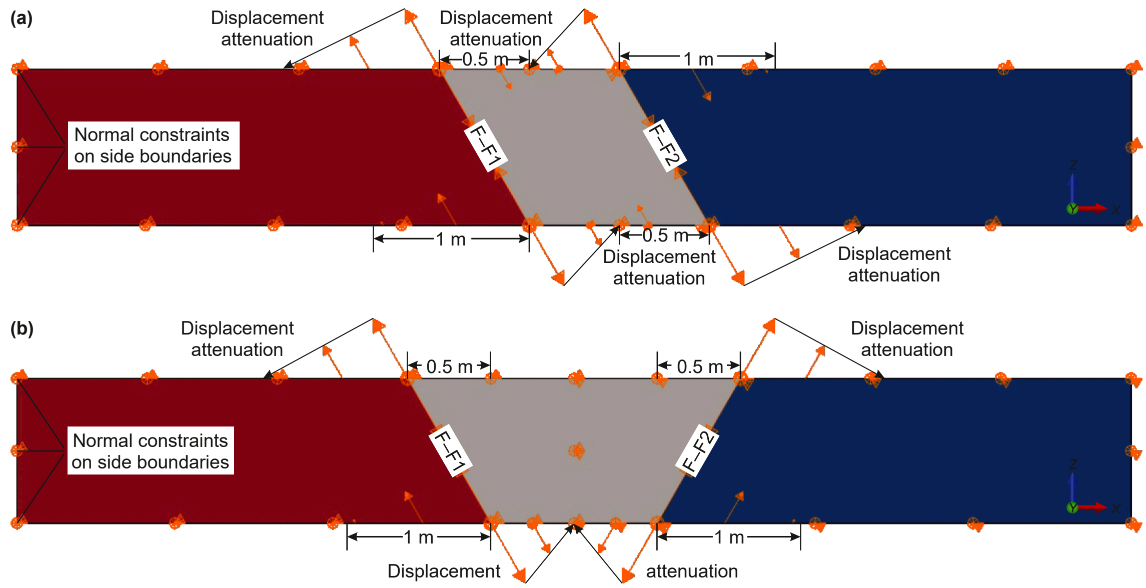

Fig. 13. Loading methods of double F–F models. (**a**) Model with two identically inclined F–Fs. (**b**) Model with two oppositely inclined F–Fs.

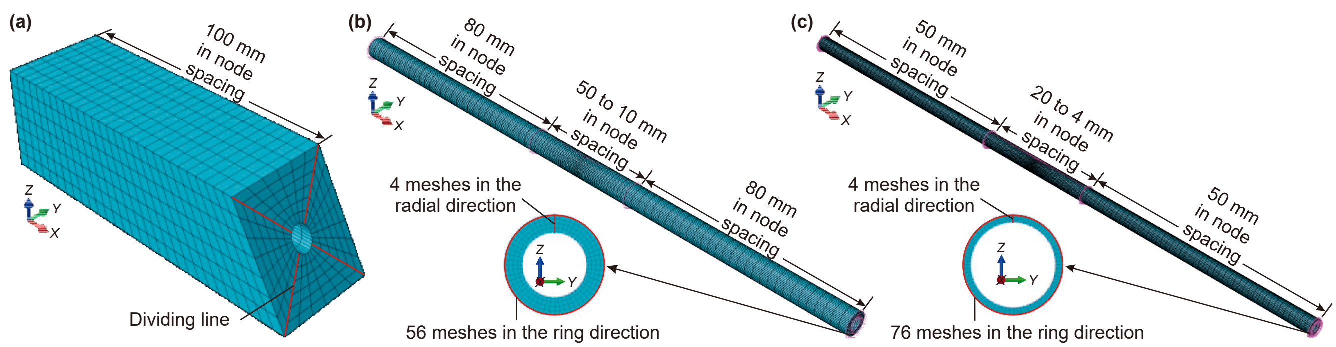

Fig. 14. Mesh divisions of different parts of the model. (**a**) Strata. (**b**) Cement sheath. (**c**) Casing.

the cement sheath are set to 80 mm, and a non-uniform refinement mode from 50 mm at the edges to 10 mm at the center is set on both sides of the F–F plane, with 56 meshes in the ring direction and 4 meshes in the radial direction (Fig. 14(b)). The axial mesh node spacings of the casing are set to 50 mm, and a non-uniform density mode from 20 mm at the edges to 4 mm at the center is set on both sides of the F–F plane, with 76 meshes in the ring direction and 4 meshes in the radial direction (Fig. 14(c)). The purpose of axial local mesh refinement is to coordinate the relationship between simulation accuracy and calculation amount, making the simulation results more accurate without increasing the calculation amount too much.

3.7. Analysis of simulation results

The analysis of simulation results is carried out in three aspects: CS–CD morphology, the measurement of CD amount and CD length, and the influence parameters of CD amount.

3.7.1. Analysis of CS–CD morphology

First, the simulation results in the displacement uniformity mode and displacement attenuation mode are compared. When observed locally from the contact of the F–F, cement sheath and casing, there is basically no difference in the CS–CD morphology simulated by the two (Fig. 15): the casing is subjected to asymmetric compression deformation by the shear action of the strata on both F–F sides, resulting in intensive twist and hole shrinkage of the casing and misalignment of the casing axis. However, if observed from the overall perspective of lateral shortening, the simulation results of the displacement attenuation mode are obviously more in line with the actual CS–CD morphology characteristics: The closer to the F–F plane, the more significant the CS–CD is. The casing axis is misaligned near the F–F plane, and toward both F–F sides, the casing gradually returns to its normal form, and the casing axis returns to its original position (Fig. 16(b)), rather than the overall misalignment of the casing axis in the displacement uniformity mode (Fig. 16(a)).

Then, the simulation results of the double F–F models are analyzed. In both models, the local deformation morphology of the casing near the F–F plane is no different from that of single F–F models. However, from the overall perspective of lateral shortening, the casing axes of the models with two identically inclined F–Fs and two oppositely inclined F–Fs show stepped and centrosymmetric misalignment respectively, and toward the F–F-free regions on both sides, the casings gradually return to their normal form, and the casing axes return to their original positions (Fig. 17). The two types of CD morphology are not only very similar to those documented in the literature (Guo et al., 2019; Xi et al., 2019; Zhang et al., 2021b, 2023), but also similar to the seismic event morphology in domino and graben structures in seismic profiles (Fig. 18). It should be noted that due to spatial constraints, simultaneous slip of two F–Fs (especially two oppositely inclined

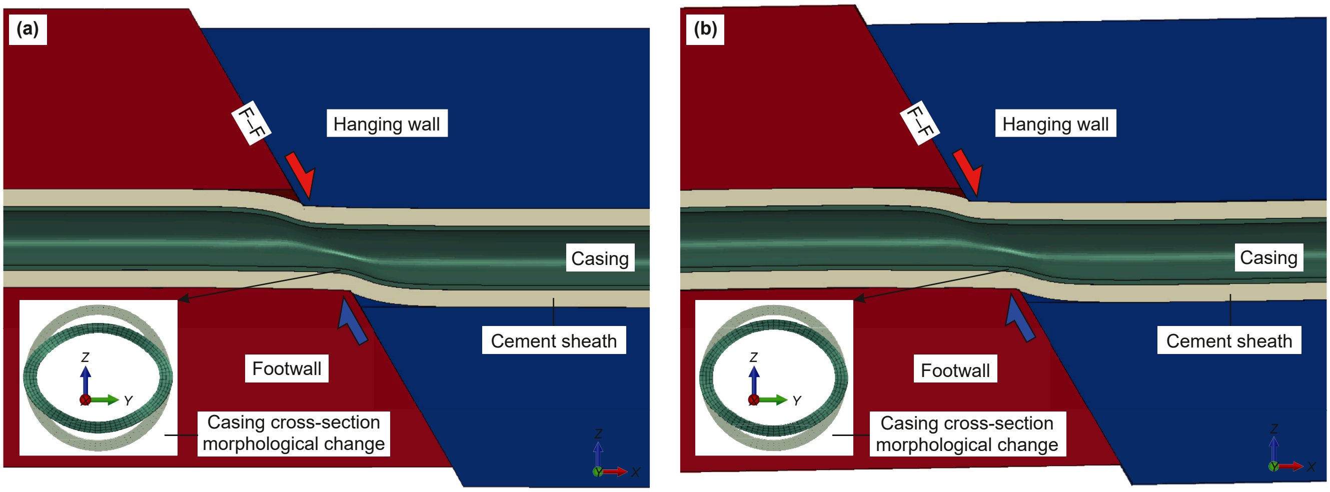

Fig. 15. Comparison of the casing local morphology in the simulation results under different loading methods. (**a**) Displacement uniformity mode. (**b**) Displacement attenuation mode with a displacement attenuation distance of 1 m.

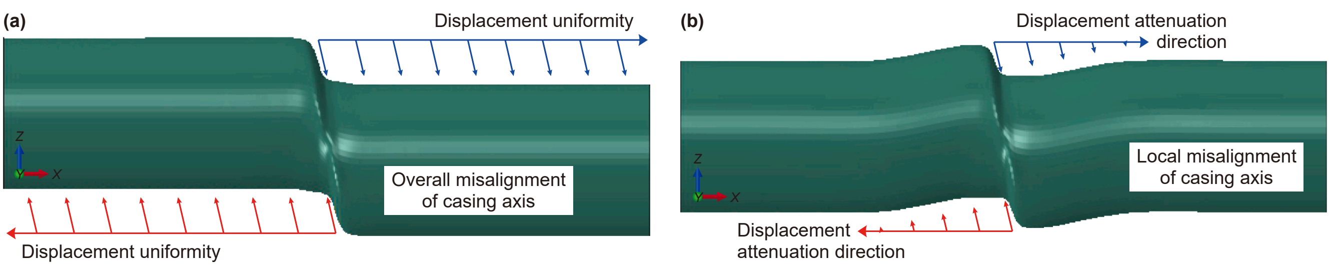

Fig. 16. Comparison of the casing overall morphology (laterally shortened to 1/10 of the original length) in the simulation results under different loading methods. (**a**) Displacement uniformity mode. (**b**) Displacement attenuation mode with a displacement attenuation distance of 1 m.

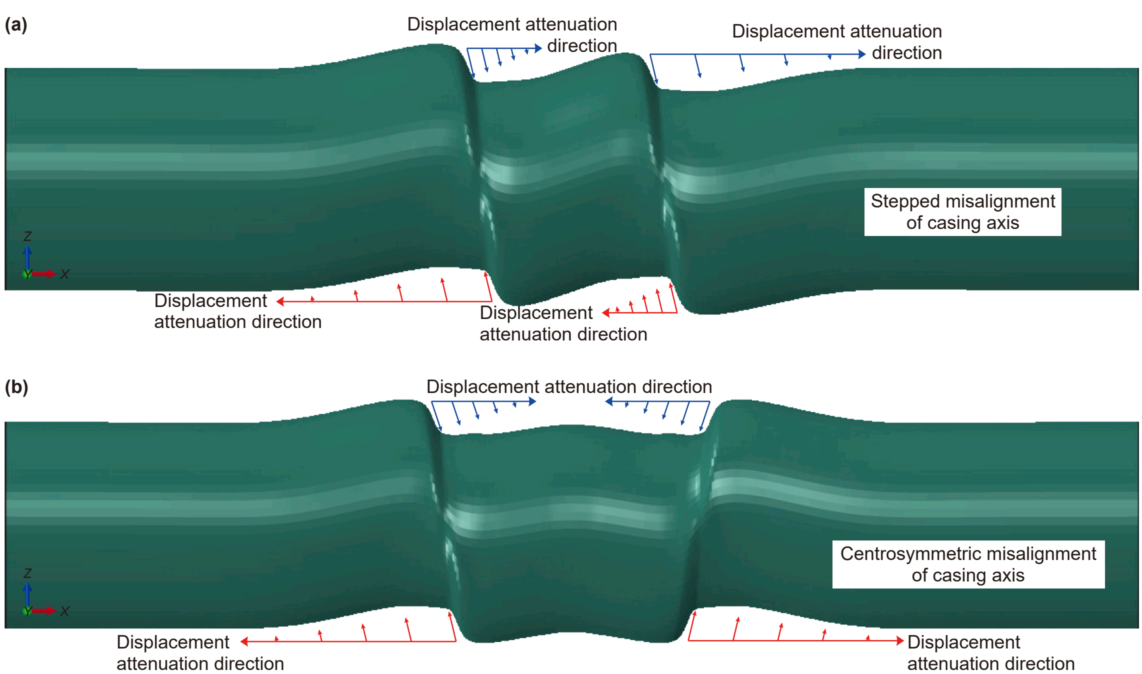

Fig. 17. Comparison of the casing overall morphology (laterally shortened to 1/10 of the original length) in the simulation results of the double F–F models. (**a**) Model with two identically inclined F–Fs. (**b**) Model with two oppositely inclined F–Fs.

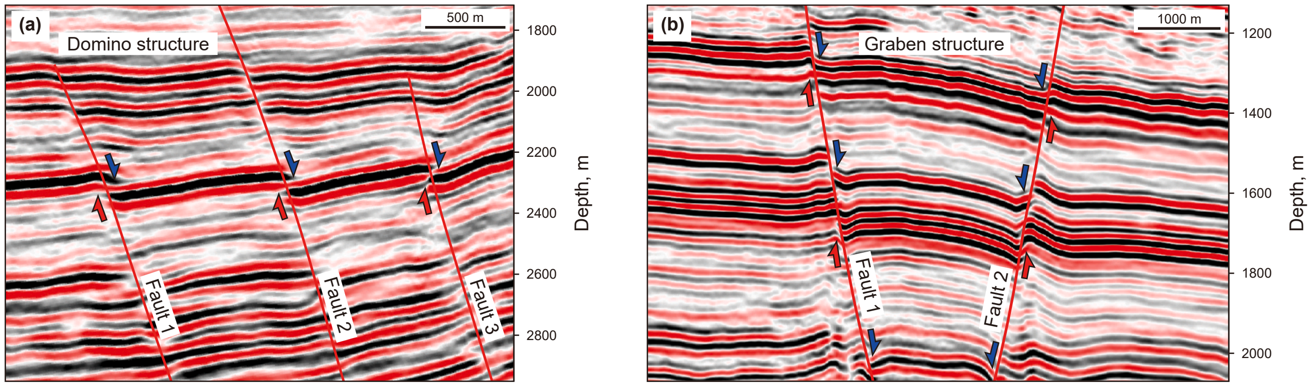

Fig. 18. Domino and graben structures in seismic profiles in the Gulong block of the Songliao Basin. (**a**) Three identically inclined normal faults form a domino structure, and the dislocated seismic events show stepped misalignment. (**b**) Two oppositely inclined normal faults form a graben structure, and the dislocated seismic events show centrosymmetric misalignment.

F–Fs) or even multiple F–Fs within a short distance (e.g., 10 m) is less likely. Therefore, the occurrence of these two types of CD morphology is correspondingly less frequent.

The above analysis shows that the displacement attenuation mode is consistent with the kinematic characteristics of F–F slip that induces CS–CD, and the CS–CD morphology characteristics in the results of the CS–CD numerical simulations adopting the displacement attenuation mode as a boundary condition are also very similar to the actual CD morphology characteristics.

3.7.2. Analysis of the measurement of the CD amount and CD length

As mentioned above, predecessors consider that the CD amount is the change in the casing inner diameter at the intersection between the casing and the F–F plane before and after CD, rather than the change in the casing drift diameter that allows the pipe string tool to pass through before and after CD. Therefore, the CD amount measured in this way will be significantly smaller than the actual CD amount. Currently, similar problems exist in the CD amount measurement using MIT in the field, i.e., the difference between the minimum inner diameter of the CD section and the original inner diameter is regarded as the CD amount. For example, in a horizontal well in the Weiyuan gas field, casings with an inner diameter of 114.3 mm were used, and the measured CD amount in a casing section was 9.3 mm through MIT, while for the ϕ99 bridge plug used for fracturing, the minimum casing drift diameter that it can pass through 102 mm, i.e., the maximum CD amount that allows the bridge plug to pass through, is 12.3 mm. Therefore, according to the measurement results of the MIT, the bridge plug should pass through normally here, but the actual situation is that the bridge plug was blocked here. This suggests that the CD amount measurement methods adopted, both in the literature and in the field, are incorrect.

In fact, since the downhole pipe string tool, including the bridge plug and perforation gun during hydraulic fracturing, is up to several meters long with a nonequally external diameter, and material stiffness issues also need to be considered, there is currently a lack of measurement and calculation methods for accurate casing drift diameter. Therefore, we improved the measurement method of the CD amount in this paper, i.e., the change in the vertical distance between the two points with the closest vertical distance on the casing inner wall after CD ((AA′–DD′) in Fig. 3) is regarded as the CD amount. In this way, it is equivalent to considering the pipe string tool to be of infinite length and uniform external diameter. Considering that the pipe string tool is several meters long, the CD amount (AA′–DD′) measured by this measurement method will be slightly smaller than the actual CD amount (AA′–BB′) and significantly smaller than the CD amount (AA′–CC′) measured by the change in local casing inscribed circle diameter. Since the longer the pipe string tool, the closer (AA′–DD′) will be to (AA′–BB′), it is obvious that this CD amount measurement method will have a much smaller deviation when the actual pipe string tool is several meters long. Accordingly, the analysis of the influence parameters of the CD amount obtained by this measurement method will be more realistic.

Due to the lack of an accurate calculation method for casing drift diameter, we cannot directly conclude how much the error can be reduced with this measurement method compared to the previous one. However, the CD amount in the above CD section is 14.1 mm measured by this measurement method, which corresponds to the actual situation that the bridge plug was blocked here. In the simulation results of models with displacement attenuation distances of 1 m and 2 m (Fig. 19), the CD amount measured by this measurement method are 31.6 and 37.2 mm respectively, while the CD amount measured by the change in local casing inscribed circle diameter are 21.4 and 24.9 mm respectively. This indicates that there is an evident difference between the CD amounts measured by the two measurement methods, and the new one provides a more accurate reflection of the actual CD amount.

In addition, since the CS–CD simulations conducted by predecessors were carried out under the displacement uniformity mode, the simulated casings only deform at their intersection with F–F planes, and thus, the CD lengths are only a few tens of centimeters long (Fig. 16(a)). In the simulation results of the displacement attenuation mode, the CD lengths are equal to the casing lengths where the casing axes on both F–F sides are misaligned, i.e., the casing twisted parts are also calculated in the CD lengths. In the simulation results of models with displacement attenuation distances of 1 m and 2 m, the CD lengths are 2.5 m and 4.9 m respectively (Fig. 19). This indicates that the smaller the F–F displacement attenuation rate, the longer the casing length where the casing axis is misaligned, which explains the phenomenon that the CD length can reach several meters or even more than 10 m. According to statistics, 32% of CD sections in the Weiyuan block are less than 5 m, 34% of those are 5–10 m, and 34% of those are greater than 10 m. By adjusting the displacement attenuation distance, the displacement attenuation model can easily simulate long CD sections with very low errors. However, the CD length of the traditional displacement uniformity model is only 0.5 m (Fig. 16(a)),

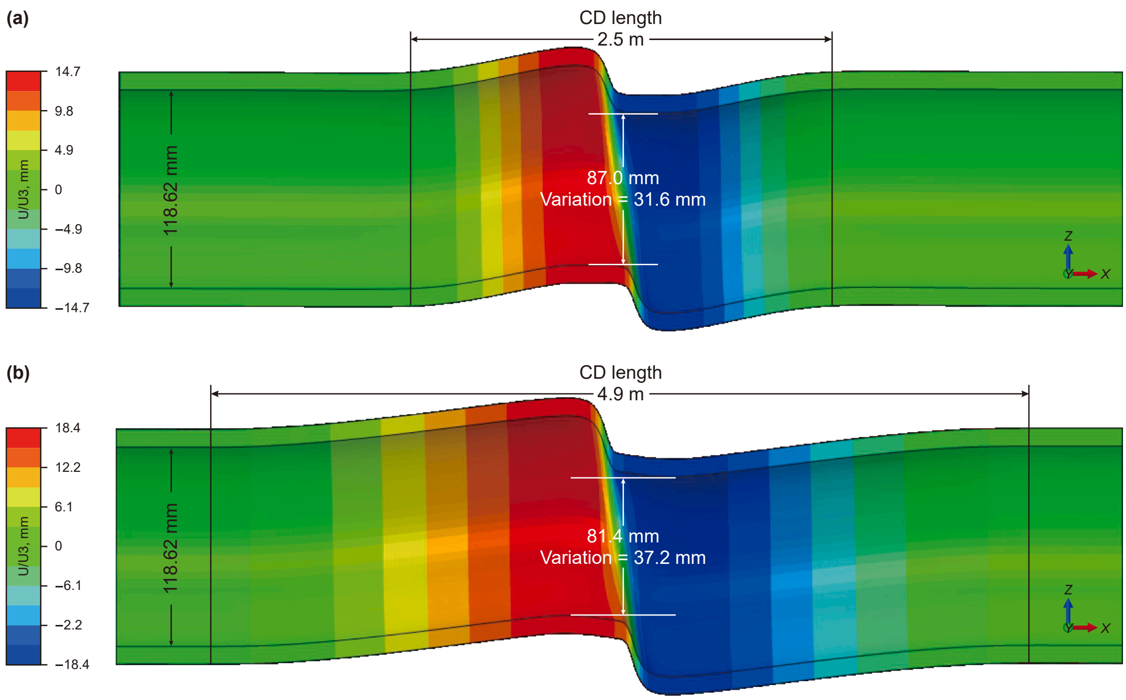

Fig. 19. Comparison of the displacement magnitude distribution in the *Z* direction (laterally shortened to 1/10 of the original length) in the simulation results of models with different displacement attenuation distances. (**a**) Model with a displacement attenuation distance of 1 m. (**b**) Model with a displacement attenuation distance of 2 m. In the figure, "U/ U3" is the displacement magnitude in the *Z* direction.

which is obviously inconsistent with the actual situation. This further verifies the rationality of the displacement attenuation model.

3.7.3. Analysis of the influence parameters of the CD amount

According to the above CD amount measurement, the CD amount (C) of 46 models is measured and counted. In each model, the total F–F slip amount is 50 cm, the CD amount is measured for every 10 cm increase in the F–F slip amount, and each model will obtain five data points of the CD amounts (Table 3). These data are then plotted as curve graphs of the relationships between the CD amount and each parameter variable. The simulation results show that the CD amount is basically linearly positively correlated with the F–F slip amount, is positively correlated with the angle between the F–F strike and the well trajectory and with the F–F dip angle and is basically independent of the stratum Young's modulus and Poisson's ratio, the cement sheath Young's modulus, Poisson's ratio and wall thickness, and the casing yield strength and wall thickness, and that the increase in the casing yield strength and wall thickness will not lead to a significant change in the F–F slip amount endured by the casing when it yields (D_y) (Fig. 20).

Since the vertical displacement component of F–F slip is linearly positively correlated with the F–F slip amount, the CD amount is also basically linearly positively correlated with the F–F slip amount (Fig. 20(a)). Since the vertical displacement component of F–F slip is (nonlinearly) positively correlated with the angle between the F–F strike and the well trajectory and the F–F dip angle, the CD amount is also basically positively correlated with the angle between the F–F strike and the well trajectory and the F–F dip angle (Fig. 20(b) and (c)).

As a rigid constraint, the strata have a weak deformation capacity under general geological conditions. Therefore, changes in the stratum Young's modulus and Poisson's ratio will not significantly change the CD amount: when the F–F slip amount is 50 mm and E_1 decreases from 40 to 20 GPa, C decreases from 37.4 to 37.2 mm, with a decrease of 0.2 mm (Fig. 20(d)); when the F–F slip amount is 50 mm and υ_1 decreases from 0.3 to 0.2, C decreases from 37.2 to 36.9 mm, with a decrease of 0.3 mm (Fig. 20(e)).

As a consolidation material between the strata and casing, the deformation capacity of the cement sheath is slightly greater than that of the strata. However, under general engineering technical conditions, changes in the cement sheath Young's modulus, Poisson's ratio and wall thickness will also not significantly change the CD amount: when the F–F slip amount is 50 mm and E_2 decreases from 10 to 0.1 GPa, C decreases from 37.2 to 33.8 mm, with a decrease of 3.4 mm (Fig. 20(f)); when the F–F slip amount is 50 mm and υ_2 decreases from 0.3 to 0.22, C decreases from 37.2 to 37.1 mm, with a decrease of 0.1 mm (Fig. 20(g)); when the F–F slip amount is 50 mm and L_1 increases from 38.1 to 60 mm, C decreases from 37.2 to 37.1 mm, with a decrease of 0.1 mm (Fig. 20(h)). It can be seen that the continuous reduction of the cement sheath Young's modulus will cause the cement sheath to deform to a greater extent during the F–F slip, thereby reducing the CD amount. However, under general engineering technical conditions, this reduction is still not significant and cannot meet engineering requirements of CD prevention.

Since the stress concentration generated on the casing during the F–F slip will quickly exceed the casing yield strength, when the casing yield strength and wall thickness are increased, the F–F slip amount corresponding to the casing yield point changes and the CD amount will not significantly change: when the F–F slip amount is 50 mm and σ_s increases from 800 to 1000 GPa, C decreases from 37.2 to 37.1 mm, with a decrease of 0.1 mm, and D_y increases from 2.1 to 2.6 mm, with an increase of 0.5 mm (Fig. 20(i) and (k)). When the F–F slip amount is 50 mm and L_2 increases from 10.54 to 20 mm, C decreases from 37.2 mm to 36.7 mm, with a decrease of 0.5 mm and D_y increases from 2.3 to 2.8 mm, with an increase of 0.5 mm (Fig. 20(j) and (l)).

Table 3
Statistics for the CD amount in the simulation results of CS–CD models.

Model number	α, °	φ, °	L_1, mm	L_2, mm	E_1, GPa	υ_1	E_2, GPa	υ_2	σ_s, MPa	C, mm				
										$D = 10$ mm	$D = 20$ mm	$D = 30$ mm	$D = 40$ mm	$D = 50$ mm
1	90	60	38.1	10.54	20	0.3	10	0.25	864	7.4	14.8	22.2	29.6	37.2
2	90	60	38.1	10.54	20	0.3	8	0.25	864	7.4	14.8	22.2	29.6	37.2
3	90	60	38.1	10.54	20	0.3	6	0.25	864	7.5	14.8	22.2	29.6	37.2
4	90	60	38.1	10.54	20	0.3	4	0.25	864	7.5	14.8	22.2	29.6	37.1
5	90	60	38.1	10.54	20	0.3	2	0.25	864	7.5	14.8	22.1	29.4	36.9
6	90	60	38.1	10.54	20	0.3	1	0.25	864	7.5	14.7	21.9	29.2	36.5
7	90	60	38.1	10.54	20	0.3	0.1	0.25	864	6.7	13.4	20.2	27.0	33.8
8	90	60	38.1	10.54	20	0.3	10	0.3	864	7.4	14.8	22.2	29.7	37.2
9	90	60	38.1	10.54	20	0.3	10	0.28	864	7.4	14.8	22.2	29.6	37.2
10	90	60	38.1	10.54	20	0.3	10	0.26	864	7.4	14.8	22.2	29.6	37.2
11	90	60	38.1	10.54	20	0.3	10	0.24	864	7.4	14.8	22.2	29.6	37.1
12	90	60	38.1	10.54	20	0.3	10	0.22	864	7.4	14.8	22.2	29.6	37.1
13	90	60	38.1	10.54	25	0.3	10	0.25	864	7.5	14.8	22.2	29.7	37.3
14	90	60	38.1	10.54	30	0.3	10	0.25	864	7.5	14.9	22.3	29.8	37.3
15	90	60	38.1	10.54	35	0.3	10	0.25	864	7.5	14.9	22.3	29.8	37.4
16	90	60	38.1	10.54	40	0.3	10	0.25	864	7.5	14.9	22.3	29.9	37.4
17	90	60	38.1	10.54	20	0.2	10	0.25	864	7.4	14.7	22.1	29.5	36.9
18	90	60	38.1	10.54	20	0.22	10	0.25	864	7.4	14.7	22.1	29.5	37.0
19	90	60	38.1	10.54	20	0.24	10	0.25	864	7.4	14.7	22.1	29.5	37.0
20	90	60	38.1	10.54	20	0.26	10	0.25	864	7.4	14.8	22.1	29.6	37.1
21	90	60	38.1	10.54	20	0.28	10	0.25	864	7.4	14.8	22.2	29.6	37.1
22	90	60	38.1	10.54	20	0.3	10	0.25	800	7.4	14.8	22.2	29.7	37.2
23	90	60	38.1	10.54	20	0.3	10	0.25	850	7.4	14.8	22.2	29.6	37.2
24	90	60	38.1	10.54	20	0.3	10	0.25	900	7.4	14.8	22.2	29.6	37.1
25	90	60	38.1	10.54	20	0.3	10	0.25	950	7.5	14.8	22.2	29.6	37.1
26	90	60	38.1	10.54	20	0.3	10	0.25	1000	7.5	14.8	22.2	29.6	37.1
27	90	60	38.1	12	20	0.3	10	0.25	864	7.4	14.8	22.1	29.6	37.1
28	90	60	38.1	14	20	0.3	10	0.25	864	7.4	14.8	22.1	29.5	37.0
29	90	60	38.1	16	20	0.3	10	0.25	864	7.4	14.7	22.1	29.4	36.9
30	90	60	38.1	18	20	0.3	10	0.25	864	7.4	14.7	22.0	29.4	36.8
31	90	60	38.1	20	20	0.3	10	0.25	864	7.4	14.7	22.0	29.3	36.7
32	90	60	40	10.54	20	0.3	10	0.25	864	7.4	14.8	22.2	29.6	37.2
33	90	60	45	10.54	20	0.3	10	0.25	864	7.4	14.8	22.2	29.6	37.2
34	90	60	50	10.54	20	0.3	10	0.25	864	7.4	14.8	22.2	29.6	37.1
35	90	60	55	10.54	20	0.3	10	0.25	864	7.4	14.8	22.2	29.6	37.1
36	90	60	60	10.54	20	0.3	10	0.25	864	7.4	14.8	22.2	29.6	37.1
37	75	60	38.1	10.54	20	0.3	10	0.25	864	7.4	14.6	21.9	29.3	36.7
38	60	60	38.1	10.54	20	0.3	10	0.25	864	7.0	14.0	21.0	28.0	34.9
39	45	60	38.1	10.54	20	0.3	10	0.25	864	6.3	12.6	18.8	25.0	31.2
40	30	60	38.1	10.54	20	0.3	10	0.25	864	4.8	9.6	14.3	19.1	23.8
41	15	60	38.1	10.54	20	0.3	10	0.25	864	2.1	4.1	6.1	8.1	10.0
42	90	90	38.1	10.54	20	0.3	10	0.25	864	8.4	16.9	25.5	34.1	42.8
43	90	75	38.1	10.54	20	0.3	10	0.25	864	8.2	16.4	24.6	33.0	41.4
44	90	45	38.1	10.54	20	0.3	10	0.25	864	6.1	12.1	18.1	24.0	30.0
45	90	30	38.1	10.54	20	0.3	10	0.25	864	4.0	7.9	11.8	15.6	19.4
46	90	15	38.1	10.54	20	0.3	10	0.25	864	0.5	0.9	1.4	2.2	3.0

4. Discussion

4.1. S-shaped CD caused by the local reduction in the cement sheath Young's modulus

Although the CS–CD morphology shown in Fig. 16(b) is generally similar to that in the actual situation (Fig. 1), there are still some differences in local details. Specifically, the casing surfaces of some CD sections are still relatively smooth, although the casings strongly twist (Fig. 21(a)), and the casings as a whole show S-shaped deformation without the sharp edges shown in Fig. 16(b). We believe that during F–F slip, the cement sheath and even the strata, at their intersections with the F–F plane, will be locally broken at positions subjected to the shear-compression action due to the stress concentration effect, which will lead to an obvious reduction in their Young's modulus here. Following this idea, we designed a model to briefly analyze the phenomenon.

In this model, the displacement attenuation mode with a displacement attenuation distance of 1 m is adopted for the boundary load. The cement sheath Young's modulus at positions subjected to the shear-compression action reduces to 0.1 GPa and gradually returns to 10 GPa toward 1 m away from the F–F plane on both F–F sides. The remaining parameters of this model are taken as non-model variables. Judging from the simulation result (Fig. 21(b)), the casing in the CD section obviously becomes smoother, and the sharp edges disappear, which is very similar to Fig. 18(a). This indicates that during F–F slip, the reduction in the cement sheath Young's modulus at its intersection with the F–F plane will indeed cause the CD morphology to show a smooth S-shaped deformation.

4.2. Guidance of simulation results for the CD prevention

First, compared with the traditional displacement uniformity model, which will lead to the inconsistency between the CD morphology and the actual situation and the severe underestimation of the CD length, the simulation results of models based on the displacement attenuation law revealed in this paper match the actual CD morphology and length. This not only further elucidates the geomechanical mechanism of CD caused by F–F slip, but also

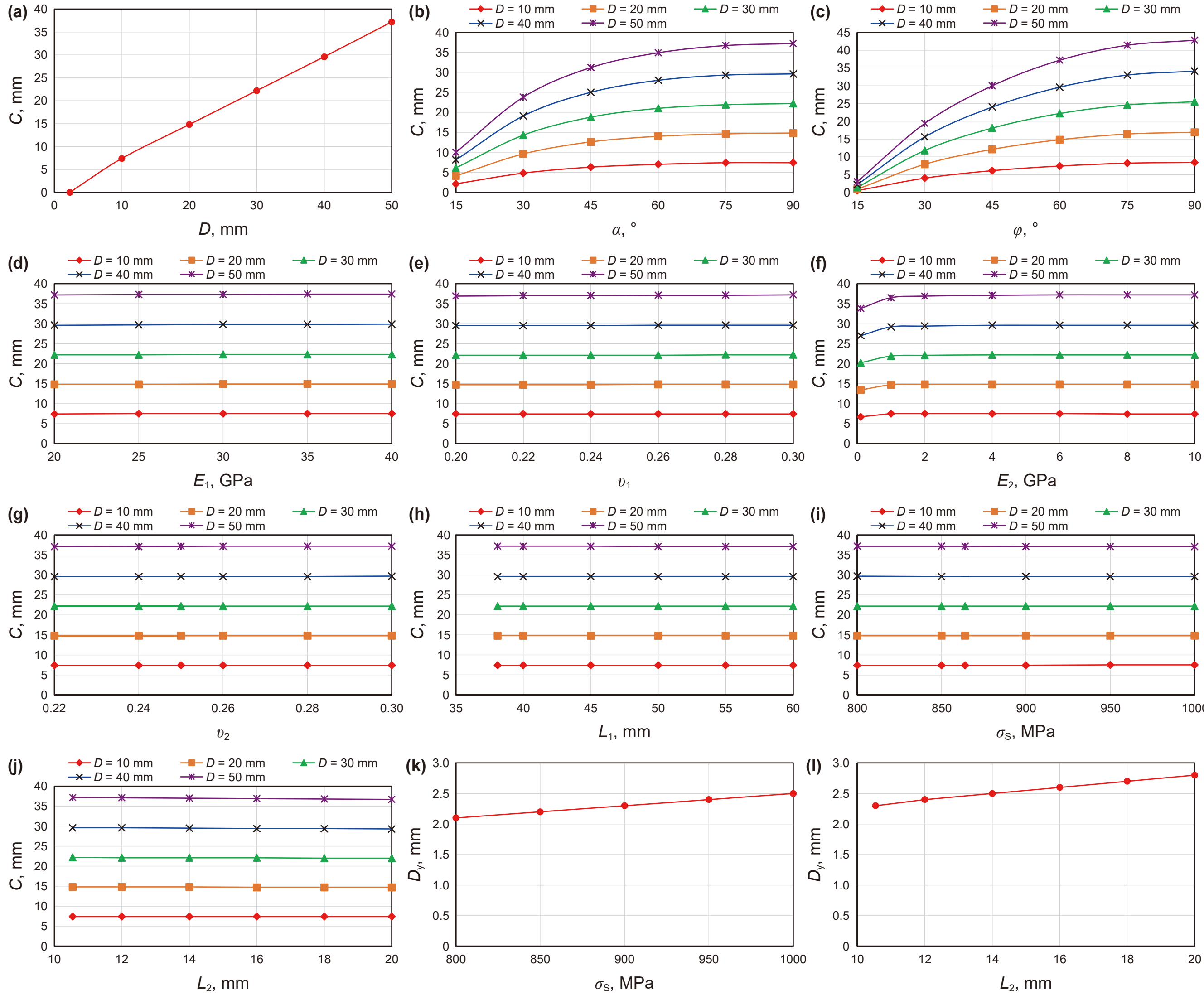

Fig. 20. Curve graphs of the relationships between the CD amount and each parameter variable. (**a**) C–D. (**b**) C–α. (**c**) C–φ. (**d**) C–E_1. (**e**) C–υ_1. (**f**) C–E_2. (**g**) C–υ_2. (**h**) C–L_1. (**i**) C–σ_S. (**j**) C–L_2. (**k**) D_y–σ_S. (**l**) D_y–L_2.

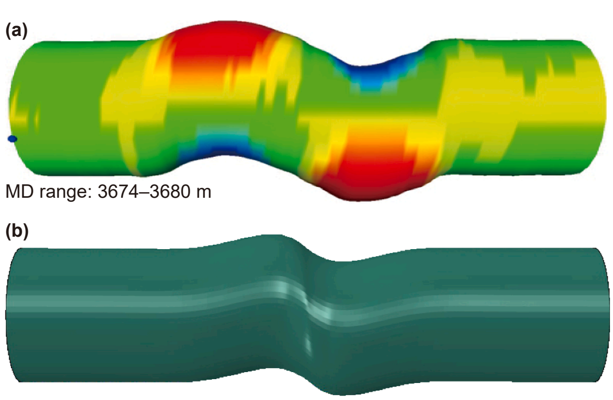

Fig. 21. Comparison between the S-shaped CD morphology of the MIT-24 interpretation and the simulation result (lateral shortened to 1/10 of the original length). (**a**) 3D morphology of MIT-24 interpretation in the 3674–3680 m section of well W4H40-8, with the same color scale as Fig. 1. (**b**) Overall CD morphology in the simulation result of the model with a local reduction in the cement sheath Young's modulus.

points out the direction of subsequent CD prevention work: adopt appropriate engineering measures to prevent or moderate the impact of F–F slip on the casing during hydraulic fracturing. Specific measures may include optimizing the fracturing scale before fracturing, composite temporary plugging during fracturing, and reasonable flowback after fracturing, etc. (Tong et al., 2021a; Zhang et al., 2021a, 2023) to reduce the possibility of F–F slip, thereby balancing production increase and the CD risk.

Second, the simulation results show that the CD amount is basically independent of the casing steel grade (mainly affecting the yield strength) and wall thickness and that increasing the casing steel grade and wall thickness will not lead to a significant change in the F–F slip amount endured by the casing when it yields. This is mainly because when the F–F slip is impeded by the cement sheath and casing, a significant stress concentration will form at the intersection of the three, and with the increase in the F–F slip amount, the stress on the casing will rapidly exceed its yield strength and cause CD. Therefore, under the current technical conditions, no matter how strong the casing is, it cannot resist the

F–F slip, which further demonstrates that the practice of increasing the casing steel grade and wall thickness to prevent CD is not feasible and matches the field test results that the CD rate did not decrease but increased after using the casing of high steel grade and thick wall in the Weiyuan gas field (Tong et al., 2021b; Zhang et al., 2021a).

Finally, the simulation results also show that the CD amount is basically independent of the cement sheath Young's modulus and wall thickness. At the F–F slip amount of 50 mm, the CD amounts in the models with the cement sheath Young's modulus of 10 GPa and 0.1 GPa are 37.2 mm and 33.8 mm respectively, the latter decreasing by 9.1% compared to the former. Although this decrease is not large, it is foreseeable that when the cement sheath Young's modulus continues to decrease, such as when using ultra-flexible cement with properties close to fluid materials for cementing or even without cementing, the CD amount will decrease more significantly, and increasing the cement sheath wall thickness at this time will also further decrease the CD amount. In addition, some scholars (Cao et al., 2022; Yang et al., 2023) have proposed using cement with hollow ceramic particles for cementing so that the F–F slip amount can be partly absorbed by the crushing of hollow ceramic particles, which is equivalent to decreasing the cement sheath Young's modulus. However, when using these means to prevent CD, factors such as F–F identification accuracy, cementing quality and operation cost need to be comprehensively considered.

5. Conclusions

Through the above simulations, analyses and discussions, the following conclusions are drawn in this paper:

(1) The strata on both F–F sides will undergo movements with displacement attenuation from the F–F plane to both F–F sides during F–F slip.
(2) The improved displacement attenuation model successfully reproduces the actual CS–CD morphology. Displacement attenuation is the root cause of the existence of long CD sections.
(3) The CD amount depends on the change in the casing drift diameter, and the CD length is negatively correlated with the F–F displacement attenuation rate.
(4) The CD amount is basically linearly positively correlated with the F–F slip amount, is positively correlated with the angle between the F–F strike and the well trajectory and with the F–F dip angle and is basically independent of the stratum Young's modulus and Poisson's ratio, the cement sheath Young's modulus, Poisson's ratio and wall thickness, and the casing yield strength and wall thickness. Increasing the casing steel grade and wall thickness is ineffective in preventing CD.

Based on the research results, this paper suggests adopted measures such as using special flexible materials to set buffers during cementing, optimizing the fracturing scale before fracturing, composite temporary plugging during fracturing, and reasonable flowback after fracturing to prevent or moderate the impact of F–F slip on the casing during hydraulic fracturing, thereby preventing CD.

CRediT authorship contribution statement

Hong-Xiang Zhang: Writing – original draft, Visualization, Software, Methodology, Investigation, Conceptualization. **Heng-Mao Tong:** Writing – review & editing, Validation, Project administration, Methodology, Conceptualization. **Wen-Hai Ma:** Supervision, Project administration, Funding acquisition, Formal analysis. **Nan Zhang:** Validation, Project administration, Formal analysis, Data curation. **Ping Zhang:** Supervision, Resources, Project administration, Data curation. **Zi-Ping Liu:** Validation, Resources, Funding acquisition, Formal analysis. **Peng Wang:** Supervision, Project administration, Funding acquisition. **Shu-Lin Li:** Visualization, Validation, Investigation. **Yuan Neng:** Writing – review & editing, Methodology, Conceptualization. **Cheng-Lin Liu:** Writing – review & editing, Validation, Methodology. **Xue-Song Li:** Visualization, Validation, Data curation. **Liang Zhang:** Project administration, Resources.

Declaration of competing interest

The authors declare that they have no known competing financial interests or personal relationships that could have appeared to influence the work reported in this paper.

Acknowledgements

We thank the Exploration Research Project of CNPC Daqing Oilfield Company Limited (No. 2021-35), the Major Science and Technology Project of CNPC (No. 2019F-31) and Xinjiang Uygur Autonomous Region Key R&D Special Project (No. 2024B01015-3) for supporting this paper.

Nomenclature

CD	Casing deformation
CS–CD	Casing shear–compression deformation
MIT	Multi-finger Imaging Tool
F–F	Small fault and large fracture
σ_{ij}	Stress tensor component
ε_{ij}	Strain tensor component
E	Young's modulus, Pa
υ	Poisson's ratio
σ_1, σ_2, σ_3	Maximum, intermediate, and minimum principal stresses
τ	Friction stress
σ_n	Normal stress
μ	Friction coefficient
D	F–F slip amount, m
α	Angle between the F–F strike and the well trajectory
φ	F–F dip angle
L_1	Wall thickness of the cement sheath, m
L_2	Wall thickness of the casing, m
E_1	Young's modulus of the strata, Pa
υ_1	Poisson's ratio of the strata
E_2	Young's modulus of the cement sheath, Pa
υ_2	Poisson's ratio of the cement sheath
σ_s	Yield strength of the casing, Pa
C	CD amount, m
D_y	F–F slip amount endured by the casing when it yields, m

References

Cao, J., Yang, S.Y., Han, L.H., et al., 2022. Research on casing deformation prevention technology of a deep shale gas well based on cementing slurry system optimization. Processes 10 (9), 1678. https://doi.org/10.3390/pr10091678.
Chen, Z.W., Zhou, L., Walsh, R., et al., 2018. Case study: Casing deformation caused by hydraulic fracturing-induced fault slip in the Sichuan Basin. In: Unconventional Resources Technology Conference. Society of Exploration Geophysicists, American Association of Petroleum Geologists. Society of Petroleum Engineers, Houston, Texas, USA. https://doi.org/10.15530/urtec-2018-2882313.

Daneshy, A.A., 2005. Impact of off-balance fracturing on borehole stability and casing failure. In: The 2005 SPE Western Regional Meeting. Irvine, California, USA. https://doi.org/10.2118/93620-MS.

Davis, G.H., Reynolds, S.J., Kluth, C.F., 2011. Structural geology of rocks and regions. John Wiley & Sons.

Dong, K., Liu, N.Z., Chen, Z.W., et al., 2019. Geomechanical analysis on casing deformation in Longmaxi shale formation. J. Pet. Sci. Eng. 177, 724–733. https://doi.org/10.1016/j.petrol.2019.02.068.

Fossen, H., 2016. Structural Geology 2nd. Cambridge university press.

Guo, X.L., Li, J., Liu, G.H., et al., 2019. Numerical simulation of casing deformation during volume fracturing of horizontal shale gas wells. J. Pet. Sci. Eng. 172, 731–742. https://doi.org/10.1016/j.petrol.2018.08.067.

Hill, R., 1950. The mathematical theory of plasticity. Oxford University Press.

Jaeger, J.C., Cook, N.G.W., Zimmerman, R.W., 2007. In: Fundamentals of rock mechanics, fourth ed. Wiley-Blackwell.

Jiang, K., Li, Q., Chen, Y.L., et al., 2015. Influence of cementing quality on casing failures in horizontal shale gas wells. Nat. Gas. Ind. 35 (12), 77–82. https://doi.org/10.3787/j.issn.1000-0976.2015.12.012 (in Chinese).

Li, Z., Li, H.T., Li, G., et al., 2021. The influence of shale swelling on casing deformation during hydraulic fracturing. J. Pet. Sci. Eng. 205, 108844. https://doi.org/10.1016/j.petrol.2021.108844.

Lian, Z.H., Yu, H., Lin, T.J., et al., 2015. A study on casing deformation failure during multi-stage hydraulic fracturing for the stimulated reservoir volume of horizontal shale wells. J. Nat. Gas Sci. Eng. 23, 538–546. https://doi.org/10.1016/j.jngse.2015.02.028.

Liu, Y.H., Zhang, J.T., Bai, J., et al., 2023. Numerical study of hydraulic fracturing in the sectorial well-factory considering well interference and stress shadowing. Pet. Sci. 20 (6), 3567–3581. https://doi.org/10.1016/j.petsci.2023.05.020.

Shen, X.P., 2014. Numerical estimation of casing integrity under injection pressure for fracturing of shale gas formation. In: Shale Energy Engineering 2014. https://doi.org/10.1061/9780784413654.034. Pittsburgh, Pennsylvania, USA.

Shi, C.S., Wang, A., Zhu, X.H., et al., 2023. Casing shear deformation mechanism and prevention measures of multifault slip induced by shale gas volume fracturing. J. Pipeline Syst. Eng. 14 (4), 4023035. https://doi.org/10.1061/JPSEA2.PSENG-1370.

Sugden, C., Johnson, J., Chambers, M., et al., 2012. Special considerations in the design optimization of high rate, multistage fractured shale wells. In: IADC/SPE Drilling Conference and Exhibition. San Diego, California, USA. https://doi.org/10.2118/151470-MS.

Tian, Z.L., Shi, L., Qiao, L., Research of and countermeasure for wellbore integrity of shale gas horizontal well. Nat. Gas. Ind. 35(9), 70-76. https://doi.org/10.3787/j.issn.1000-0976.2015.09.010 (in Chinese).

Timoshenko, S.P., Goodier, J.N., 1951. In: Theory of Elasticity, second ed. McGraw-Hill.

Tong, H.M., Chen, Z.L., Liu, R.X., 2015. Generalized shear activation criterion. Zi Ran Za Zhi 37 (6), 441–447. https://doi.org/10.3969/j.issn.0253-9608.2015.06.007 (in Chinese).

Tong, H.M., Cai, D.S., Wu, Y.P., et al., 2010. Activity criterion of pre-existing fabrics in non-homogeneous deformation domain. Sci. China: Earth Sci. 53, 1115–1125. https://doi.org/10.1007/s11430-010-3080-6.

Tong, H.M., Liu, Z.P., Zhang, H.X., et al., 2021a. Theory and method of temporary macrofracture plugging to prevent casing deformation in shale gas horizontal wells. Nat. Gas. Ind. 41 (5), 92–100. https://doi.org/10.3787/j.issn.1000-0976.2021.05.010 (in Chinese).

Tong, H.M., Yin, A., 2011. Reactivation tendency analysis: A theory for predicting the temporal evolution of preexisting weakness under uniform stress state. Tectonophysics 503 (3–4), 195–200. https://doi.org/10.1016/j.tecto.2011.02.012.

Tong, H.M., Zhang, P., Zhang, H.X., et al., 2021b. Geomechanical mechanisms and prevention countermeasures of casing deformation in shale gas horizontal wells. Nat. Gas. Ind. 41 (1), 189–197. https://doi.org/10.3787/j.issn.1000-0976.2021.01.017 (in Chinese).

Twiss, R.J., Moores, E.M., 2007. In: Structural Geology, second ed. WH Freeman.

Van Der Pluijm, B.A., Marshak, S., 2004. Earth Structure: An Introduction to Structural Geology and Tectonics. WW Norton.

Xi, Y., Li, J., Liu, G.H., et al., 2018. Numerical investigation for different casing deformation reasons in Weiyuan-Changning shale gas field during multistage hydraulic fracturing. J. Pet. Sci. Eng. 163, 691–702. https://doi.org/10.1016/j.petrol.2017.11.020.

Xi, Y., Li, J., Zha, C.Q., et al., 2019. A new investigation on casing shear deformation during multistage fracturing in shale gas wells based on microseism data and calliper surveys. J. Pet. Sci. Eng. 180, 1034–1045. https://doi.org/10.1016/j.petrol.2019.05.079.

Yang, S.Y., Zeng, B., Yan, Y., et al., 2023. Research on casing deformation mechanism and prevention technology in salt rock creep formation. J. Pet. Sci. Eng. 220, 111176. https://doi.org/10.1016/j.petrol.2022.111176.

Yin, F., Gao, D.L., 2015. Prediction of sustained production casing pressure and casing design for shale gas horizontal wells. J. Nat. Gas Sci. Eng. 25, 159–165. https://doi.org/10.1016/j.jngse.2015.04.038.

Yin, F., Han, L.H., Yang, S.Y., et al., 2018. Casing deformation from fracture slip in hydraulic fracturing. J. Pet. Sci. Eng. 166, 235–241. https://doi.org/10.1016/j.petrol.2018.03.010.

Yu, H., Lian, Z.H., Lin, T.J., 2014. Numerical simulation of influence of cementing quality on casing failure for oil field. Comput. Simulat. 31 (9), 161–164. https://doi.org/10.3969/j.issn.1006-9348.2014.09.035 (in Chinese).

Zhang, Z., Tang, J.Z., Zhang, J.T., et al., 2024. Modeling of scale-dependent perforation geometrical fracture growth in naturally layered media. Eng. Geol. 336, 107499. https://doi.org/10.1016/j.enggeo.2024.107499.

Zhang, F.S., Jiang, Z.Y., Chen, Z.W., et al., 2020. Hydraulic fracturing induced fault slip and casing shear in Sichuan Basin: A multi-scale numerical investigation. J. Pet. Sci. Eng. 195, 107797. https://doi.org/10.1016/j.petrol.2020.107797.

Zhang, H.X., Tong, H.M., Zhang, P., et al., 2023. How can casing deformation be prevented during hydraulic fracturing of shale gas? —A case study of the Weiyuan area in Sichuan, China. Geoenergy Sci. Eng. 221, 111251. https://doi.org/10.1016/j.petrol.2022.111251.

Zhang, P., He, Y.B., Liu, Z.P., et al., 2021a. Shear compression deformation test and deformation prevention practice of casing in shale gas horizontal wells. Nat. Gas. Ind. B 8 (5), 514–522. https://doi.org/10.1016/j.ngib.2021.08.008 (in Chinese).

Zhang, X., Li, J., Zhang, H., et al., 2021b. Analysis of casing deformation failure mechanism based on fault slip. Eng. Fail. Anal. 127, 105430. https://doi.org/10.1016/j.engfailanal.2021.105430.